

Response and resistance to BET bromodomain inhibitors in triple-negative breast cancer

Shaokun Shu^{1,2*}, Charles Y. Lin^{1,2*}, Housheng Hansen He^{1,2,3,4,5*}, Robert M. Witwicki^{1,2*}, Doris P. Tabassum¹, Justin M. Roberts¹, Michalina Janiszewska^{1,2}, Sung Jin Huh^{1,2}, Yi Liang⁴, Jeremy Ryan^{1,2}, Ernest Doherty^{1,6}, Hisham Mohammed⁷, Hao Guo³, Daniel G. Stover^{1,2}, Muhammad B. Ekram^{1,2}, Guillermo Peluffo^{1,2}, Jonathan Brown^{1,2}, Clive D'Santos⁷, Ian E. Krop^{1,2}, Deborah Dillon^{1,8}, Michael McKeown^{1,2}, Christopher Ott^{1,2}, Jun Qi^{1,2}, Min Ni^{1,2}, Prakash K. Rao⁹, Melissa Duarte⁹, Shwu-Yuan Wu¹⁰, Cheng-Ming Chiang¹⁰, Lars Anders¹¹, Richard A. Young¹¹, Eric P. Winer^{1,2}, Antony Letai^{1,2}, William T. Barry^{2,3}, Jason S. Carroll⁷, Henry W. Long^{1,9}, Myles Brown^{1,2,9}, X. Shirley Liu^{3,9,12}, Clifford A. Meyer³, James E. Bradner^{1,2,12} & Kornelia Polyak^{1,2,9,12}

Triple-negative breast cancer (TNBC) is a heterogeneous and clinically aggressive disease for which there is no targeted therapy^{1–3}. BET bromodomain inhibitors, which have shown efficacy in several models of cancer^{4–6}, have not been evaluated in TNBC. These inhibitors displace BET bromodomain proteins such as BRD4 from chromatin by competing with their acetyl-lysine recognition modules, leading to inhibition of oncogenic transcriptional programs^{7–9}. Here we report the preferential sensitivity of TNBCs to BET bromodomain inhibition *in vitro* and *in vivo*, establishing a rationale for clinical investigation and further motivation to understand mechanisms of resistance. In paired cell lines selected for acquired resistance to BET inhibition from previously sensitive TNBCs, we failed to identify gatekeeper mutations, new driver events or drug pump activation. BET-resistant TNBC cells remain dependent on wild-type BRD4, which supports transcription and cell proliferation in a bromodomain-independent manner. Proteomic studies of resistant TNBC identify strong association with MED1 and hyper-phosphorylation of BRD4 attributable to decreased activity of PP2A, identified here as a principal BRD4 serine phosphatase. Together, these studies provide a rationale for BET inhibition in TNBC and present mechanism-based combination strategies to anticipate clinical drug resistance.

To explore non-oncogene addiction to BRD4 in breast cancer, we studied a series of BET bromodomain inhibitors (BBI) across breast cell lines reflecting transcriptionally defined breast cancer subtypes: luminal, HER2⁺ and TNBC^{2,10}, as well as MCF10A and MCF12A basal/mesenchymal immortalized mammary epithelial cells (Supplementary Table 1). Potent inhibitory effects were observed preferentially in TNBC lines, compared to more resistant luminal lines (Fig. 1a). Analysis of potency of drug response and subtype or known driver mutations identified the basal subtype as the only significant association ($P=0.0475$) (Supplementary Table 1 and data not shown). BRD4 dependency was confirmed by RNA interference and phenocopied BBI (Extended Data Fig. 1a–c). JQ1 or BRD4 knockdown induced growth inhibition and resulted in G1 arrest and apoptosis (Extended Data Fig. 1d–g). Expression of factors described to mediate JQ1 effect (MYC) or required for TNBC growth (JAK2/STAT3) showed no clear association with JQ1 sensitivity (Extended Data Fig. 1h and Extended Data Fig. 2a, b). JQ1 treatment of TNBC cells induced significant morphologic

changes consistent with induction of senescence, confirmed by β-galactosidase staining and luminal differentiation evidenced by changes in the expression of basal and luminal markers (Extended Data Fig. 2c, d and Fig. 1b).

Extending the translational significance of these findings, we evaluated the ability of JQ1 to inhibit tumour growth in murine TNBC xenografts. Two-week treatment efficiently inhibited established tumour growth from SUM159 and MDA-MB-231 lines, and patient-derived primary human TNBC xenografts (Fig. 1c and Extended Data Fig. 2e, f). Downregulation of BRD4 using two independent TET-inducible short hairpin RNAs produced even more pronounced effects, leading to complete tumour regression and failure to regrow even after discontinuing doxycycline treatment (Fig. 1c and Extended Data Fig. 2g). Evidence of BBI-induced basal-to-luminal differentiation was confirmed *in vivo* (Extended Data Fig. 2f, h).

Using integrated epigenomic analysis (Supplementary Table 2), we identified the direct transcriptional targets of BBI in TNBC. BBI binding was identified at active promoter and enhancer regions using ChemSeq¹¹ for biotinylated JQ1 (Bio-JQ1) enrichment and chromatin immunoprecipitation followed by sequencing (ChIP-seq) for acetyl-histone (H3K27ac) and BRD4 enrichment, with the three marks showing near perfect co-localization (Fig. 1d and Extended Data Fig. 3a). BBI efficiently displaced chromatin-bound BRD4 in treated SUM159 (Fig. 1e and Extended Data Fig. 3b) and in SUM149 cells (Extended Data Fig. 3c). To identify biologically relevant direct targets of BBI in SUM159 and SUM149 cells, we quantified binding of Bio-JQ1 and BRD4 genome-wide and found strong enrichment at 219 and 159 super-enhancers, respectively (Fig. 1f, Extended Data Fig. 3d and Supplementary Table 3)^{8,9,12,13}. Transcription factors with known roles in breast cancer, such as POU5F1B/MYC¹⁴ and HIF1α¹⁵, were evident among top super-enhancer-associated genes in both lines. Kinetic effects of JQ1 treatment on gene expression demonstrated preferential super-enhancer-associated gene downregulation (Fig. 1g and Extended Data Fig. 3e, f). Expression changes were observed within 3 h after JQ1 treatment and, as expected, more genes were significantly down- than upregulated (Extended Data Fig. 3g–j and Supplementary Table 4). Unsupervised Metacore¹⁶ analysis of JQ1-affected target pathways revealed downregulation of regulatory and effector genes in anti-apoptotic and JAK/STAT signalling pathways (Extended Data Fig. 3k).

¹Department of Medical Oncology, Dana-Farber Cancer Institute, Boston, Massachusetts 02215, USA. ²Department of Medicine, Brigham and Women's Hospital, and Department of Medicine, Harvard Medical School, Boston, Massachusetts 02115, USA. ³Department of Biostatistics and Computational Biology, Dana-Farber Cancer Institute, and Department of Biostatistics, Harvard School of Public Health, Boston, Massachusetts 02115, USA. ⁴Princess Margaret Cancer Center/University Health Network, Toronto, Ontario M5G1L7, Canada. ⁵Department of Medical Biophysics, University of Toronto, Toronto, Ontario M5G2M9, Canada. ⁶Harvard University, Cambridge, Massachusetts 02138, USA. ⁷Cancer Research UK, Cambridge Institute, University of Cambridge, Cambridge CB2 0RE, UK. ⁸Department of Pathology, Brigham and Women's Hospital, and Department of Pathology, Harvard Medical School, Boston, Massachusetts 02115, USA. ⁹Center for Functional Cancer Epigenetics, Dana-Farber Cancer Institute, Boston, Massachusetts 02215, USA. ¹⁰Simmons Comprehensive Cancer Center, Departments of Biochemistry and Pharmacology, University of Texas Southwestern Medical Center, Dallas, Texas 75390, USA. ¹¹Whitehead Institute for Biomedical Research, Cambridge, Massachusetts 02142, USA. ¹²Broad Institute, Cambridge, Massachusetts 02142, USA.

*These authors contributed equally to this work.

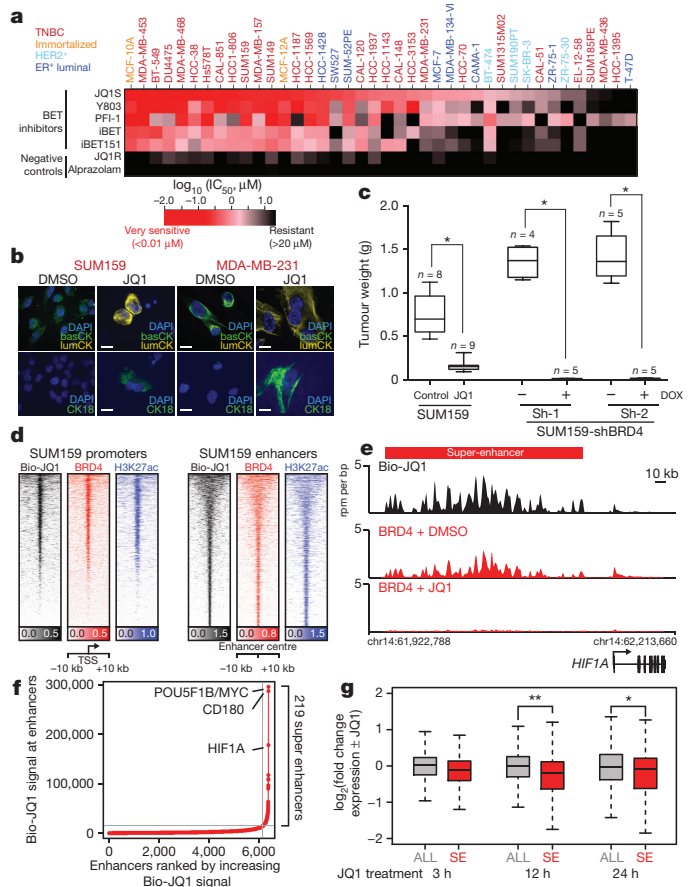


Figure 1 | Response to BBIs in breast cancer. **a**, Heat map of mean IC_{50} s of BBIs and inactive analogues in breast cell lines. Error bars represent s.e.m. **b**, Immunofluorescence of basal (basCK) and luminal (lumCK and CK18) cytokeratins in TNBC lines. Scale bars, 20 μ m. **c**, Box plots depicting xenograft weights; n indicates the number of mice per experiment. * $P < 0.0001$ (unpaired t -test). **d**, Heat map showing biotinylated JQ1 (Bio-JQ1), BRD4 and H3K27ac binding at transcription start site (TSS) and Bio-JQ1-bound enhancer regions. Each row represents a single genomic region (± 10 kb) from TSS or enhancer centre. Genomic occupancy is shaded by binding intensity in units of reads per million per base pair (rpm per bp). **e**, Gene tracks depicting Bio-JQ1 and BRD4 with or without JQ1 in SUM159 cells at the *HIF1A* locus. x -axis, chromosome position with gene structures below; y -axis, genomic occupancy in units of rpm per bp; red bar, *HIF1A* super-enhancer. **f**, Plot of enhancers defined in untreated SUM159 cells ranked by increasing Bio-JQ1 signal (units rpm). Grey line marks cut-off discriminating typical from super-enhancers. **g**, Box plots showing the \log_2 fold change in expression relative to control of either all active or super-enhancer (SE)-associated genes upon JQ1 treatment. ** $P < 10^{-5}$ (Welsh's t -test); * $P < 10^{-3}$ (Welsh's t -test).

These data support selective disruption of super-enhancer-associated genes by JQ1, leading to deregulation of coordinated transcriptional pathways involved in cell proliferation, invasion and survival.

Dissecting resistance to targeted therapy is critical to elucidate mechanisms of drug and target action, and to suggest approaches to treat or anticipate drug resistance in patients. Therefore, we established BBI-resistant TNBC cell lines by long-term culture of both SUM159 and SUM149 cells in escalating JQ1 doses. Low (0.5 μ M) and high (2.0 μ M) doses of JQ1 severely impaired proliferation of parental SUM159 and SUM149 lines, reducing viable cells after 6 days (Fig. 2a and Extended Data Fig. 3l). In contrast, JQ1-resistant cells (SUM159R and SUM149R) proliferated linearly, even in high JQ1 doses (20 μ M) (Fig. 2a and Extended Data Fig. 3l). BBI-resistance is not attributable to drug export, as MDR1 and other transporters are not transcriptionally upregulated (Extended Data Fig. 4a), co-incubation with MDR1

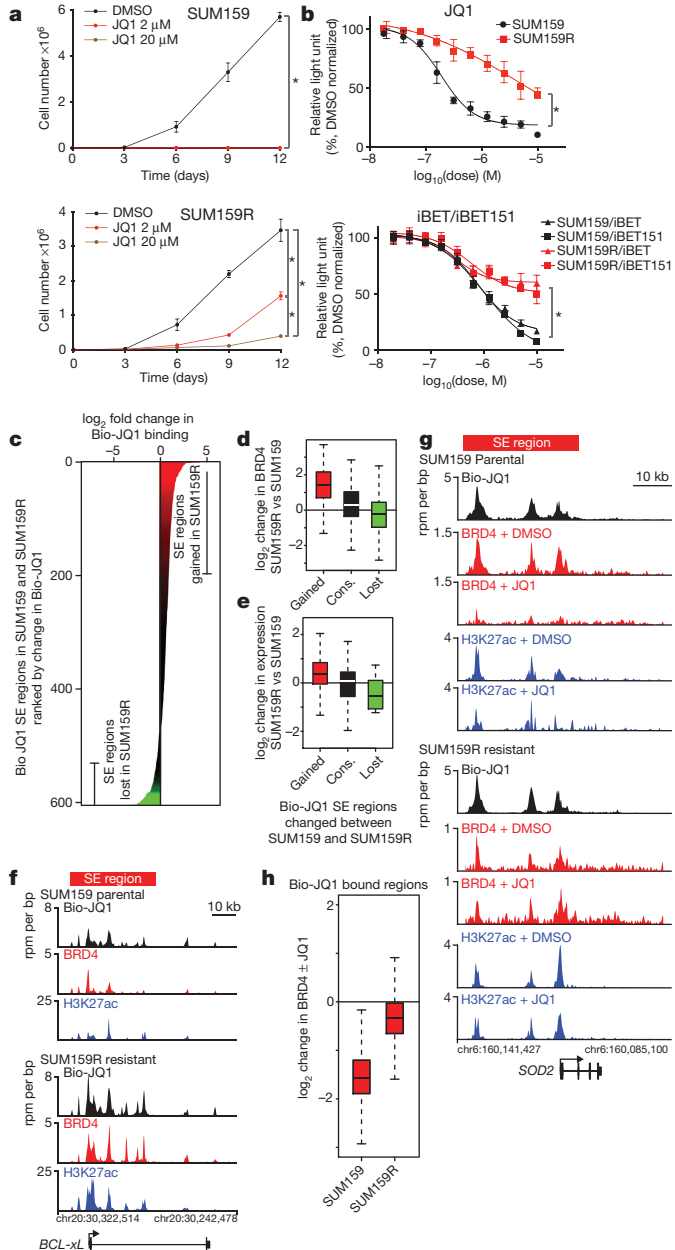


Figure 2 | Acquired BBI-resistance in TNBC. All error bars represent s.d., $n = 3$. **a**, Viable cell numbers after JQ1 treatment. * $P < 0.0001$ (two-way ANOVA). **b**, Cellular viability after treatment with BBIs. * $P < 0.0001$ (non-linear regression, extra sum-of-squares test). **c**, Genomic regions containing a super-enhancer in SUM159 or SUM159R cells ranked by \log_2 change in Bio-JQ1 genomic binding signal. x -axis, \log_2 fold change in Bio-JQ1 signal coloured by intensity of change. **d**, **e**, Box plot showing the \log_2 fold change in BRD4 genomic occupancy (d) and gene expression (e) at regions with gained, conserved, or lost Bio-JQ1 binding in SUM159 versus SUM159R cells. **f**, **g**, Gene tracks depicting Bio-JQ1, BRD4, and H3K27ac at the *BCL-XL* (also known as *BCL2L1*; f) and *SOD2* (g) locus. The x -axis shows position along the chromosome with gene structures drawn below. The y -axis shows genomic occupancy in units of rpm per bp. **h**, Box plot showing the \log_2 fold change in BRD4 genomic occupancy at regions bound by Bio-JQ1.

inhibitors (verapamil) had no effect (Extended Data Fig. 4b), and structurally divergent BBIs are equally inactive as JQ1 (Fig. 2b). Further support is provided by the equivalent chromatin engagement of BRD4 in sensitive and resistant cells, demonstrated by binding with Bio-JQ1 (Extended Data Fig. 4c). Notably, BBI-resistant TNBC cells retain sensitivity to compounds from orthogonal active drug classes, such as

CXCR2 and JAK2 inhibitors¹⁷, establishing specific resistance to BBIs (Extended Data Fig. 4d). Adaptive drug resistance was not attributable to outgrowth of a minor subpopulation of pre-existing resistant cells, as 10 independent single-cell-derived clones showed similar resistance profiles to pooled SUM159R cells (Extended Data Fig. 4e). Similar results were obtained *in vivo*, as SUM159R-derived xenografts were JQ1-unresponsive (Extended Data Fig. 4f). In all resistant TNBC populations studied, exome sequencing failed to identify alterations in BET bromodomain-encoding genes (for example, gatekeepers) or known driver genes (parallel pathway activation) (Supplementary Table 5).

Absent new genetic alterations, we explored the plausibility of an epigenomic mechanism of resistance. Differential enhancer analysis revealed a significant gain of super-enhancers in resistant SUM159R cells (Fig. 2c and Supplementary Table 6). The gain of Bio-JQ1 super enhancers was associated with enrichment for BRD4 binding to these genomic loci (Fig. 2d) and increased transcription of associated genes (Fig. 2e). An upstream/intragenic region of H3K27ac at the BCL-xL locus featured prominently among top gained super enhancers in SUM159R (Fig. 2f), consistent with increased BCL-xL messenger RNA and protein expression in resistant cells (Supplementary Table 7, Extended Data Fig. 4g). Functionally, cells with acquired resistance to BBI featured a concordant switch in JQ1 anti-apoptotic response based on dynamic BH3 profiling^{18,19} (Extended Data Fig. 4h).

Observing emergent enhancers in resistant cells, we assessed whether BBI-resistant TNBC cells retained non-oncogene addiction to BRD4. Notably, we observed loss of SUM159R cell viability upon BRD4 knockdown (Extended Data Fig. 5a, b). Together these studies establish persistence of BRD4 addiction despite resistance to bromodomain inhibition, establishing the plausibility of bromodomain-independent recruitment of BRD4 to enhancers in BBI-resistant TNBCs. To test this hypothesis, we performed BRD4 ChIP-seq on sensitive and resistant cells with and without JQ1. JQ1 neither displaced BRD4 from chromatin in SUM159R (Fig. 2g), nor meaningfully influenced epigenome structure by H3K27ac ChIP-seq (Extended Data Fig. 5c–g). Notably, several luminal markers (FOXA1, CD24, and luminal cytokeratins) were elevated in SUM159R cells in cell culture and *in vivo* (Extended Data Fig. 5h, i), supporting a model whereby resistance arises via essential BRD4 recruitment to chromatin in a bromodomain-independent manner. Similar observations were made in SUM149R cells and in TNBC cells inherently resistant to JQ1 (Extended Data Fig. 3h–j; Extended Data Fig. 6a–d), suggesting a general mechanism of epigenetic resistance to BBI.

To disclose potential differences in BRD4-associated complexes between sensitive and resistant SUM159 cells, we performed quantitative proteomics using RIME (rapid immunoprecipitation mass spectrometry of endogenous proteins)²⁰ with and without JQ1. Analysis of BRD4-associated proteins identified relative enrichment of MED1 and BRD3 in JQ1-treated resistant cells (Fig. 3a, Extended Data Fig. 7 and Supplementary Table 8). BRD4 immunoprecipitation followed by immunoblot for MED1 and BRD3 revealed that JQ1 efficiently displaced BRD4 from MED1 in sensitive cells, but not in resistant cells (Fig. 3b), a result confirmed in SUM149 and BBI-resistant SUM149R, as well as inherently resistant TNBC and luminal lines (Extended Data Fig. 8a). Although elevated BRD3 abundance was observed in SUM159R cells, increased association of BRD4 and BRD3 was not confirmed by immunoblot (Fig. 3b). To assess functionally whether increased recruitment of BRD4 to chromatin by MED1 underlies resistance to JQ1, we expressed an exogenous bromodomain-inactivated mutant (BDmut) with concomitant knockdown of endogenous BRD4 (Extended Data Fig. 8b, c). Downregulation of endogenous BRD4 decreased cell growth both in parental and resistant cells, which was rescued by enforced expression of wild-type BRD4 (Fig. 3c). BDmut BRD4 expression failed to rescue parental SUM159 cells, but supported growth of JQ1-resistant SUM159R consistent with an evident bromodomain-independent mechanism of BRD4 recruitment (Fig. 3c). Next, we assessed the sensitivity of cells

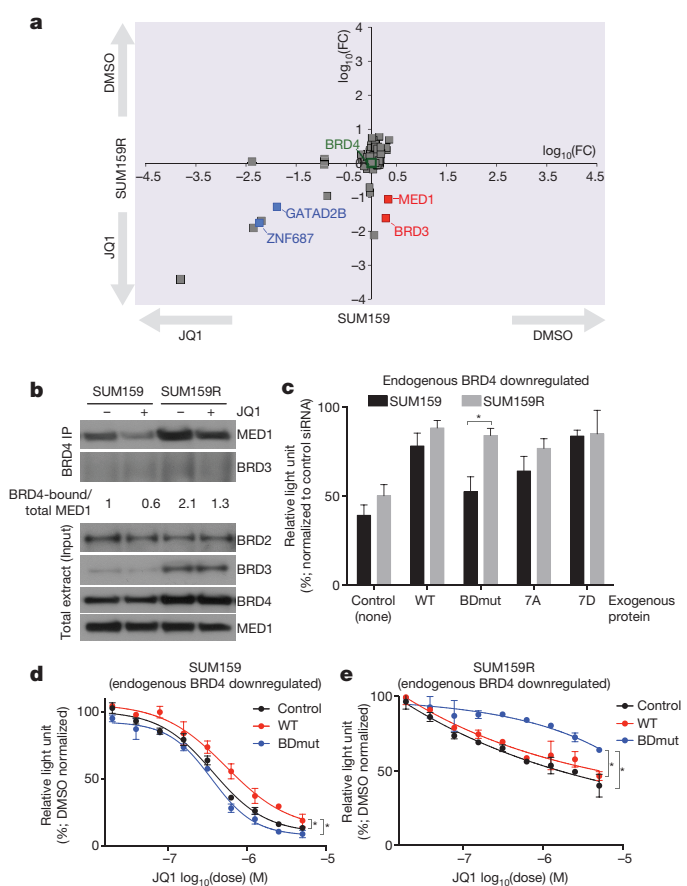


Figure 3 | Mechanism of BBI-resistance in TNBCs. All error bars represent s.d., $n = 3$. **a**, Plot depicting changes in BRD4-associated proteins in SUM159 and SUM159R cells following JQ1 treatment based on SILAC RIME. The axes represent \log_{10} of fold change (FC). **b**, Immunoblot analysis of BRD4 immunoprecipitates and total cell lysates in SUM159 and SUM159R cells. For gel source data, see Supplementary Fig. 1. **c**, Cellular viability of SUM159 and SUM159R cells expressing exogenous wild-type, BDmut, 7A and 7D mutant BRD4 with concomitant knockdown of endogenous BRD4. * $P = 0.04$ (paired t -test). **d**, **e**, Sensitivity of SUM159 (**d**) and SUM159R (**e**) cells expressing exogenous wild-type or BDmut BRD4 to JQ1 with concomitant knockdown of endogenous BRD4. * $P < 0.0001$ (non-linear regression, extra sum-of-squares test).

expressing BDmut BRD4 to JQ1, observing increased sensitivity to JQ1 in parental SUM159 cells exogenously expressing BDmut (Fig. 3d). In contrast, expression of BDmut BRD4 in SUM159R cells rescued the anti-proliferative effect of JQ1 (Fig. 3e), although this could partially be due to the slower growth of BDmut-expressing cells. Together, these studies suggest that BBI-resistance is associated with increased binding of BRD4 to MED1, in a bromodomain-independent manner unaffected by JQ1.

A recent study reported that the stability and nuclear localization of BRD4 is increased with phosphorylation by casein kinase II (CK2)²¹. To explore the contribution of BRD4 phosphorylation to BBI-resistance, we performed immunoblot analysis in parental and resistant cells and found a marked increase of phospho-BRD4 (pBRD4) in resistant cells (Fig. 4a and Extended Data Fig. 8d). Small-molecule inhibition of CK2 decreased BRD4 phosphorylation in SUM159 and SUM159R cells (Extended Data Fig. 8e). These results imply BRD4 hyperphosphorylation in resistant cells either owing to increased phosphorylation by CK2 or, alternatively, to decreased dephosphorylation by an as yet unidentified BRD4 phosphatase. We therefore first analysed CK2 activity in parental and resistant cells by performing pan-CK2 substrate immunoblots and detected no significant differences in CK2 activity (Extended Data Fig. 8f).

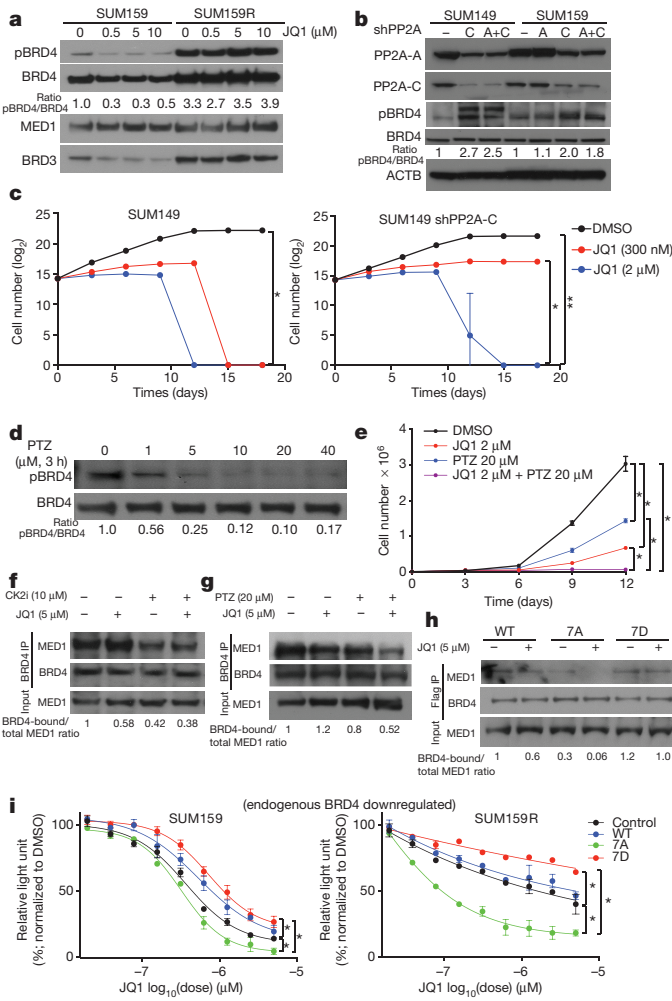


Figure 4 | Regulation and relevance of BRD4 phosphorylation. All error bars represent s.d., $n = 3$. **a**, Immunoblot for the indicated proteins following JQ1 treatment. **b**, Immunoblot for the indicated proteins after knockdown of PP2A A or C or both subunits. **c**, Viable cell numbers of JQ1-treated control and shPP2A-C expressing SUM149 cells. Left, $*P < 0.0001$ (two-way ANOVA); right, $*P = 0.0037$ and $**P = 0.0015$ (two-way ANOVA). **d**, Immunoblot of pBRD4 and BRD4 in SUM159R cells following phenothiazine (PTZ) treatment. **e**, Viable cell numbers of SUM159R cells treated with JQ1, phenothiazine or both compounds. $*P < 0.0001$ (two-way ANOVA). **f**, **g**, Immunoblot of BRD4 immunoprecipitates and total cell lysates of SUM159R cells after 3 h treatment with JQ1 and CK2i (**f**) and JQ1 and PTZ (**g**). **h**, Immunoblot of Flag-BRD4 (wild type or mutant) immunoprecipitates and total cell lysates after 3 h treatment with JQ1. **i**, JQ1 sensitivity of SUM159 and SUM159R cells expressing exogenous wild-type or mutant (7A, 7D) BRD4. $*P < 0.0001$ (non-linear regression, extra sum-of-squares test). For gel source data, see Supplementary Fig. 1.

Inactivation of the PP2A phosphatase tumour suppressor gene occurs commonly in breast cancer and is associated with therapy resistance²²; PP2A also often opposes CK2 function^{23,24}. Thus, we investigated whether PP2A may dephosphorylate BRD4 and whether decreased PP2A activity could lead to BBI resistance. Downregulation of PP2A catalytic subunit (*PPP2CA*) in SUM149 and SUM159 cells led to increased BRD4 phosphorylation, establishing PP2A as a previously unrecognized BRD4 phosphatase (Fig. 4b), further supported by pharmacologic inhibitors of PP2A that showed similar effects (Extended Data Fig. 8g). To strengthen the link between PP2A activity and BBI resistance, we tested the JQ1 sensitivity of SUM149 cells following the knockdown of PP2A C subunit and determined that downregulation of PP2A decreased JQ1 sensitivity (Fig. 4c). We have collaboratively reported phenothiazine compounds as activators of PP2A enzymatic

activity²⁵. Thus, we analysed pBRD4 levels in SUM159R, SUM149R and other cell lines after short-term treatment with phenothiazine (PTZ) and detected rapid dephosphorylation of BRD4 (Fig. 4d and Extended Data Fig. 8h). Combined treatment with PTZ and JQ1 overcame BBI resistance in SUM159R cells (Fig. 4e). To investigate the functional role of BRD4 hyperphosphorylation in BBI resistance, we analysed whether BRD4 phosphorylation influences MED1 binding. Indeed, SUM159R cells treated with CK2 inhibitor or PTZ both lead to decreased MED1 abundance in BRD4 immunoprecipitations, suggesting that pBRD4 binds MED1 more efficiently than BRD4 (Fig. 4f, g).

To functionally assess the role for BRD4 phosphorylation in BBI resistance and MED1 binding, we generated BRD4 constructs encoding mutants that cannot be phosphorylated by CK2 (7 serine to alanine substitutions; '7A mutant') or mimic constitutive phosphorylation (7 serine to aspartate substitutions; '7D mutant'). We first assessed the ability of these constructs to rescue effects of endogenous BRD4 knockdown in stable cell lines (Extended Data Fig. 8b, c). We observed expression of both 7D and 7A mutants supporting the growth of both parental SUM159 and JQ1-resistant SUM159R cells (Fig. 3c). Next, we analysed MED1 binding and subcellular localization of 7A and 7D mutants in the presence or absence of JQ1. We found that the 7A mutant displays weaker MED1 binding compared to wild-type BRD4 and completely dissociates after JQ1, whereas the 7D mutant seems to have higher affinity for MED1 that is unaffected by JQ1 treatment (Fig. 4h and Extended Data Fig. 8i). Lastly, we assessed the sensitivity of cells expressing 7A or 7D mutant BRD4 to JQ1. In parental SUM159 cells exogenously expressed 7D mutant BRD4 decreased sensitivity to JQ1, whereas the 7A mutant slightly increased sensitivity (Fig. 4i). In contrast, expression of 7A mutant BRD4 in SUM159R cells restored JQ1 sensitivity, whereas the 7D mutant showed a modest decrease. These results strongly support the hypothesis that hyperphosphorylation of BRD4 arises from decreased PP2A activity in BBI resistant cells, leading to increased binding of BRD4 to MED1, recruitment to chromatin and decreased responsiveness to bromodomain inhibition.

To explore the clinical relevance of phospho-BRD4 (pBRD4) in BET inhibitor-naïve TNBC, we performed immunofluorescence analysis of a tissue microarray (TMA) featuring of 89 patient-derived TNBC specimens. First, we validated the pBRD4 immunofluorescence assay by comparing xenografts derived from SUM159 and SUM159R cell lines and detected significantly higher pBRD4 in SUM159R cells (Extended Data Fig. 9a). We detected strong pBRD4 staining among a subset of TNBCs (Extended Data Fig. 9b, c), and variable staining overall that was not correlated with expression of the androgen receptor and basal cytokeratins (bCK; Extended Data Fig. 9d, e) and it was not significantly associated with disease outcomes (Supplementary Table 9 and Extended Data Fig. 9f).

To extend the translational relevance of our findings, we conducted synergy studies of JQ1 with molecules targeting BCL-XL (ABT737), a gained super-enhancer in SUM159R cells, and modulators of BRD4 phosphorylation, the CK2 inhibitor CX-4945 and the PP2A activator perphenazine (PPZ). We observed significant synergy between JQ1 and all three compounds studied (Extended Data Fig. 10), establishing a rationale for combination studies of BBI in TNBC to improve response and to anticipate BBI resistance.

BRD4 inhibition has demonstrated efficacy in disparate models of cancer in a rapidly expanding literature. Despite apparent resistance in the vast majority of tumour types, as we observed here in TNBC, mechanisms of BBI-resistance have not been mechanistically explained. As this research was in review, two studies reported moderate emergent resistance to BBI in murine AML associated phenotypically with a stem-like state and WNT pathway activation^{26,27}. Interestingly, in our study TNBCs with more basal/stem cell-like features and WNT pathway activation are more sensitive to BET inhibition, whereas resistant disease emerges as epigenetic adaptation to a more differentiated luminal phenotype. Our findings of persistent BET bromodomain dependency despite BBI resistance, as well as pBRD4 staining in

resistant disease, should be studied in these murine AML models and further in human leukaemia.

Integrating approaches in epigenomics, proteomics and chemical biology, we provide an example of epigenomic drug resistance by an epigenetic mechanism, where in BBI-resistant cells, decreased PP2A activity leads to hyperphosphorylated BRD4, which binds more strongly to MED1, facilitating a bromodomain-independent chromatin recruitment mechanism. This research proposes putative combination strategies to anticipate and overcome BBI resistance, including pairing with BCL-xL inhibitors (for example, ABT-737) or CK2 inhibitors, and guides the development of second-generation BBIs that disrupt BET function via orthogonal biophysical or biochemical actions. More immediately, the robust efficacy observed in pre-clinical models supports the development of BET inhibition in TNBC alone, and in combination with mechanism-based targeted therapies.

Online Content Methods, along with any additional Extended Data display items and Source Data, are available in the online version of the paper; references unique to these sections appear only in the online paper.

Received 12 November 2014; accepted 3 December 2015.

Published online 6 January 2016.

1. Vaz-Luis, I. et al. Outcomes by tumor subtype and treatment pattern in women with small, node-negative breast cancer: a multi-institutional study. *J. Clin. Oncol.* **32**, 2142–2150 (2014).
2. Lehmann, B. D. et al. Identification of human triple-negative breast cancer subtypes and preclinical models for selection of targeted therapies. *J. Clin. Invest.* **121**, 2750–2767 (2011).
3. Metzger-Filho, O. et al. Dissecting the heterogeneity of triple-negative breast cancer. *J. Clin. Oncol.* **30**, 1879–1887 (2012).
4. Puissant, A. et al. Targeting MYCN in neuroblastoma by BET bromodomain inhibition. *Cancer Discov.* **3**, 308–323 (2013).
5. Delmore, J. E. et al. BET bromodomain inhibition as a therapeutic strategy to target c-Myc. *Cell* **146**, 904–917 (2011).
6. Filippakopoulos, P. et al. Selective inhibition of BET bromodomains. *Nature* **468**, 1067–1073 (2010).
7. Belkina, A. C. & Denis, G. V. BET domain co-regulators in obesity, inflammation and cancer. *Nature Rev. Cancer* **12**, 465–477 (2012).
8. Chapuy, B. et al. Discovery and characterization of super-enhancer-associated dependencies in diffuse large B cell lymphoma. *Cancer Cell* **24**, 777–790 (2013).
9. Hnisz, D. et al. Super-enhancers in the control of cell identity and disease. *Cell* **155**, 934–947 (2013).
10. Burstein, M. D. et al. Comprehensive genomic analysis identifies novel subtypes and targets of triple-negative breast cancer. *Clin. Cancer Res.* **21**, 1688–1698 (2015).
11. Anders, L. et al. Genome-wide localization of small molecules. *Nature Biotechnol.* **32**, 92–96 (2014).
12. Lovén, J. et al. Selective inhibition of tumor oncogenes by disruption of super-enhancers. *Cell* **153**, 320–334 (2013).
13. Whyte, W. A. et al. Master transcription factors and mediator establish super-enhancers at key cell identity genes. *Cell* **153**, 307–319 (2013).
14. Hayashi, H. et al. The OCT4 pseudogene POU5F1B is amplified and promotes an aggressive phenotype in gastric cancer. *Oncogene* **34**, 199–208 (2015).
15. Semenza, G. L. HIF-1 mediates metabolic responses to intratumoral hypoxia and oncogenic mutations. *J. Clin. Invest.* **123**, 3664–3671 (2013).
16. Bessarabova, M. et al. Functional synergies yet distinct modulators affected by genetic alterations in common human cancers. *Cancer Res.* **71**, 3471–3481 (2011).
17. Marotta, L. L. et al. The JAK2/STAT3 signaling pathway is required for growth of CD44⁺CD24⁻ stem cell-like breast cancer cells in human tumors. *J. Clin. Invest.* **121**, 2723–2735 (2011).
18. Ryan, J. & Letai, A. BH3 profiling in whole cells by fluorimeter or FACS. *Methods* **61**, 156–164 (2013).
19. Montero, J. et al. Drug-induced death signaling strategy rapidly predicts cancer response to chemotherapy. *Cell* **160**, 977–989 (2015).
20. Mohammed, H. et al. Endogenous purification reveals GREB1 as a key estrogen receptor regulatory factor. *Cell Reports* **3**, 342–349 (2013).
21. Wu, S. Y., Lee, A. Y., Lai, H. T., Zhang, H. & Chiang, C. M. Phospho switch triggers Brd4 chromatin binding and activator recruitment for gene-specific targeting. *Mol. Cell* **49**, 843–857 (2013).
22. Rincón, R. et al. PP2A inhibition determines poor outcome and doxorubicin resistance in early breast cancer and its activation shows promising therapeutic effects. *Oncotarget* **6**, 4299–4314 (2015).
23. Westermarck, J. & Hahn, W. C. Multiple pathways regulated by the tumor suppressor PP2A in transformation. *Trends Mol. Med.* **14**, 152–160 (2008).
24. Eichhorn, P. J., Creyghton, M. P. & Bernards, R. Protein phosphatase 2A regulatory subunits and cancer. *Biochim. Biophys. Acta* **1795**, 1–15 (2009).
25. Gutierrez, A. et al. Phenothiazines induce PP2A-mediated apoptosis in T cell acute lymphoblastic leukemia. *J. Clin. Invest.* **124**, 644–655 (2014).
26. Rathert, P. et al. Transcriptional plasticity promotes primary and acquired resistance to BET inhibition. *Nature* **525**, 543–547 (2015).
27. Fong, C. Y. et al. BET inhibitor resistance emerges from leukaemia stem cells. *Nature* **525**, 538–542 (2015).

Supplementary Information is available in the online version of the paper.

Acknowledgements We thank D. Silver and members of the Polyak and Bradner laboratories for their critical reading of this manuscript and useful discussions. We thank G. Brown for help with creating the word cloud figures. This work was supported by the NIH DF/HCC SPORE in Breast Cancer CA168504 (K.P., E.P.W., I.E.K., D.D., W.T.B., and J.E.B.), CA080111 (K.P. and M.B.), and CA103867 (C.M.C.), Susan G. Komen Foundation (S.S.), CPRIT RP110471 and RP140367 (C.M.C.), Welch Foundation (C.M.C.), US Department of Defense CDMRP BC122003 (S.X.L.) and CA120184 (C.Y.L.), Princess Margaret Cancer Foundation (H.H.H.), Canada Foundation for Innovation and Ontario Research Fund CFI32372 (H.H.H.), NSERC discovery grant RGPIN-2015-04658 (H.H.H.), and the Harvard Ludwig Center for Cancer Research (J.E.B., M.B. and K.P.).

Author Contributions S.S. performed cell culture, xenograft, ChIP-seq, and RNA-seq experiments, and data analyses. C.Y.L. and C.A.M. performed genomic data analyses. H.H.H. helped with ChIP-seq and RNA-seq experiments and data analyses. R.M.W. performed cell culture, ChIP-seq experiments and data analyses. J.M.R. performed synergy studies. D.P.T. helped with immunofluorescence staining. M.J. and S.J.H. helped with confocal microscopy and image quantification. Y.L. helped with BRD4 ChIP-seq. M.B.E. and G.P. helped with cell cycle studies. E.D. helped with generating and testing BRD4 mutants. J.B. and L.A. performed Chem-seq. H.M., C.D. and J.S.C. conducted proteomic experiments and data analyses. C.O. and M.M. performed drug sensitivity screens. J.Q. synthesized BBI compounds. M.N. generated shRNA constructs. D.D., I.E.K. and E.P.W. generated the TMA and linked to clinical data. H.G., D.G.S. and W.T.B. performed TMA and statistical analyses. J.R. and A.L. performed BH3 profiling and data analyses. C.-M.C. and S.-Y.W. provided phospho-BRD4 antibody. P.K.R. and M.D. generated RNA-seq libraries. K.P. supervised with help from J.E.B., X.S.L., M.B., R.A.Y. and H.L. All authors helped to design the study and write the manuscript.

Author Information RNA-seq, ChIP-seq, and Chem-seq data have been deposited in the NCBI GEO database with the accession number GSE63584. Reprints and permissions information is available at www.nature.com/reprints. The authors declare competing financial interests: details are available in the online version of the paper. Readers are welcome to comment on the online version of the paper. Correspondence and requests for materials should be addressed to K.P. (kornelia_polyak@dfci.harvard.edu) or J.E.B. (james Bradner@dfci.harvard.edu).

METHODS

No statistical methods were used to predetermine sample size. The experiments were not randomized, and the investigators were not blinded to allocation during experiments and outcome assessment.

Cell lines and breast tumour tissues. Breast cell lines were obtained from the ATCC and S. Ethier (SUM series). Cells were cultured in media recommended by the provider, their identity was confirmed by STR analysis, and they were regularly tested for mycoplasma. Breast tumour samples were collected using protocols approved by the DF/HCC Institutional Review Board, informed consent was obtained from all patients. Tumours were minced with razor blades and digested with stirring for 3–4 h at 37 °C in DMEM/F12 with 2 mg ml⁻¹ BSA, 2 mg ml⁻¹ collagenase type IV, and 2 mg ml⁻¹ hyaluronidase. After digestion, cells were filtered through 500-μm mesh, washed in DMEM/F12 with 5% FBS, frozen in DMEM/F12 with 5% FBS and 10% DMSO, and stored in liquid nitrogen for subsequent xenograft studies. PDX IDC50 was derived from a primary tumour of highly invasive metaplastic TNBC resistant to chemo and radiation therapy leading to the rapid death of the patient. Exome sequencing of the tumour and xenograft identified numerous mutations including heterozygous frameshift mutation in *PTEN* (chr10_89701964-89701964_A) and *CDH1* chr16_67400242-67400242_C). PDX EL-12-58 was derived from a liver metastasis of a heavily pretreated basal-like TNBC. Oncopanel mutation testing identified homozygous mutations in *BRCA2* (p.S1970*), *TP53* (p.I232fs), *TSC2*, *FLT3*, and *ROS1*, and lower frequency mutations in *RAD21*, *JAK3*, *ARID1B*, *ARID1A*, *KDM6A*.

High-throughput screening of BET bromodomain inhibitors in breast cell line panel. We tested a panel of compounds (synthesized in the Bradner laboratory) in 40 human breast cell lines in a 384-well format at 2,000 cells per well using a semi-automated screen essentially as described⁵. Cell viability at 72 h was evaluated using ATPlite (Perkin Elmer).

Synergy studies. SUM149, SUM149R, SUM159, and SUM159R cells were seeded in sterile, white, opaque 384-well microtitre plates (Thermo), using an automated dispensing system (BioTek EL406), at 1,000 cells per well in 50 μl of media. Drugs were delivered in DMSO by robotic pin transfer with a JANUS workstation (100 nl) to achieve a matrix of pairwise dose-response incubations of each compound, each pair having eight replicates. Following 72 h of incubation, ATP levels were determined for treated cells and vehicle controls (ATPlite, PerkinElmer). Data were normalized to vehicle controls. Combination indices were determined using the median-effect principle of Chou & Talalay²⁸ (CalcuSyn Software). Isobologram plots were generated with GraphPad Prism software. Points represent paired values of drug concentrations assessed for synergism. The diagonal line signifies drug additivity. Points above the line represent antagonistic drug combinations, and those below the line represent synergistic drug combinations. Synergy assays were performed in triplicates and repeated 2–3 times.

Xenograft assays. For xenograft assays 5–6-weeks old female CrTac-NCr-*Foxn1^{Inu}* and NOD.Cg-*Prkdc^{scid}* *Il2rg^{tm1Sug}*/JicTac mice were purchased from Taconic. Tumours were induced by bilateral orthotopic mammary fat pad injection of 1 × 10⁶ cells in 50% Matrigel (BD Biosciences) in DMEM/F12 or Medium 171 (except for IDC50-X cells, which were injected with 3% FBS and 4 mg ml⁻¹ collagen gel in Medium 171). Animal experiments were conducted following protocol 11-023 approved by the Dana-Farber Cancer Institute Animal Care and Use Committee. For all the xenograft studies, the sample size of each group (5–10 mice) is indicated in the figures. We performed pilot experiments using a few (5–10) mice per group followed by larger studies if needed to reach statistical significance and repeated experiments to ensure reproducibility. Due to the nature of the performed experiments, no randomization and no blinding was used as it was deemed unfeasible. However, the resulting tumours were analysed in a blinded manner. Mice were administered JQ1 (50 mg per kg, daily), vehicle only (control) for 14 days beginning at day 14 (SUM159), or doxycycline at day 21 (SUM159-shBRD4) after injection. Mice were euthanized and tumours evaluated 28 and 60 days after injection of parental and TET-inducible shBRD4-expressing SUM159 cells into mammary fat pads.

Cellular viability, senescence, MDR and BH3 profiling assays. Cell viability and growth assays (Figs 1a, 2a, b, 3d, e, 4c, i, Extended Data Figs 1a, b, 3i, 4d, e, g, h, 10), cycle, apoptosis, and MDR assays were performed in triplicates and repeated 2–3 times. For cell proliferation assays, cells were plated at 500 cells per well in 96-well plates and treated the next day with inhibitors, DMSO or doxycycline (500 ng). Cells were cultured at 37 °C with 5% CO₂ in the media described above, and cell viability was measured using CellTiter-Glo three days after treatments. For cell growth assays, cells were plated at 5,000 (SUM159) or 20,000 (SUM149) cells per well in 6-well plates and treated the next day with inhibitors. Cells were counted every three days by cell counter. Cellular apoptosis was analysed with an APC AnnexinV/7ADD Apoptosis Detection kit (BD Pharmingen). AnnexinV/7AAD assessments and cell cycle graphics were generated using FlowJo software V7.6.1 for Windows (Tree Star). Senescence Beta-gal staining was performed using

Senescence β-Galactosidase staining kit from Cell Signaling. Briefly, after JQ1 treatment (500 nM) for 72 h, SUM159 and MDA-MB-231 cells were fixed by fixative solution for 15 min, followed by β-galactosidase solution incubation overnight at 37 °C. The staining was checked under microscope for the development of blue colour. Multi-Drug Resistance Assay was performed with MDR assay kit from Cayman Chemical (600370). Briefly, SUM159 and SUM159R cells were treated with JQ1 or DMSO for 30 min in SUM medium. Verapamil was used as a positive control at 1:1,000 dilution. Calcein AM/Hoechst Dye staining solution was added after that and cells were incubated at 37 °C for 15 min. The cells were analysed by fluorescent microscope and FACS.

Cell cycle analysis was performed 72 h after JQ1 treatment or BRD4 down-regulation with doxycycline using propidium iodide (PI) staining. Cells were resuspended in 1 ml of growth medium supplemented with 2 μg ml⁻¹ PI (Life Technologies) as final concentration. After 60 min at 37 °C in the dark, analysis was performed on a FACS AriaII cytometer (BD Biosciences). The cell cycle was plotted as histogram after excluding doublets.

Cell synchronization procedure. SUM159 cells were treated with nocodazole (200 ng ml⁻¹) for 12 h and then cells were tapped to detach from the plates. After washing twice with PBS, cells were replated with or without JQ1 in collagen-coated plates. Cells were collected at 0, 3, 6, 12 h time point for FACS and immunoblot analysis. Dynamic BH3 profiling was performed using the JC-1 plate method as previously described^{18,19}. Briefly, 2.5 × 10⁵ cells were seeded in T25 flasks in the presence of 500 nM or 5 μM JQ1 for 72 or 96 h. Cells were trypsinized, suspended in MEB (150 mM mannitol, 10 mM HEPES, 50 mM KCl, 5 mM succinate, 20 μM EDTA, 20 μM EGTA, 0.1% protease-free BSA, pH 7.5 ± 0.1), and 1–2 × 10⁴ cells were added in 15 μl of MEB to each well of a 384 well Fluotrac 200 plate containing 15 μl per well of either peptides at 2 × final concentration, buffer only, or 50 μM alamethicin in MEB supplemented with 2 μM JC-1, 10 mM 2-mercaptoethanol, 20 μg ml⁻¹ oligomycin, and 50 μg ml⁻¹ digitonin. Fluorescence at emission 590 ± 10 nM and excitation 545 ± 10 nM was recorded at 5 min intervals at 32 °C. The area under each curve was normalized to the alamethicin and buffer controls as:

$$\% \text{ Depolarization} = 1 - [(\text{AUC}_{\text{sample}} - \text{AUC}_{\text{alamethicin}})/(\text{AUC}_{\text{buffer}} - \text{AUC}_{\text{alamethicin}})]$$

Delta priming was calculated per peptide treatment as: Delta Priming = (Depolarization Treated) – (Depolarization Untreated). Positive delta priming indicates an increase in priming due to treatment and an increased potential for apoptosis at later time points.

Immunofluorescence staining and image and statistical analysis of tissue microarrays. Antibodies used for immunofluorescence were: CK18 (Dako, M7010), CK17 (Dako, M7046), HMW CK (Dako, M0630), LMW CK (Dako, M0631), CD44 (NeoMarkers, MS-668-P1), CD24 (NeoMarkers, MS-1279-P1), pSTAT3 (Cell Signaling, 9145S), VIM (Dako, M073501), CDH1 (BD Biosciences, 610181), Flag (Sigma, F1804), BrdU (Roche, 11170376001), pBRD4 (a gift from C. M. Chiang), and androgen receptor (Cell Signaling, 5153S). Immunofluorescence experiments were performed in cultured cells or in whole sections of formalin-fixed paraffin embedded (FFPE) xenograft tumours. The staining was performed as described²⁹. Antibody dilutions were as follows: pSTAT3 (1:25), CD44 (1:100), CD24 (1:100), CK18 (1:200), CK17 (1:200), HMW CK (1:100), LMW CK (1:100), VIM (1:100), CDH1 (1:100), Flag (1:50), BrdU (1:200), pBRD4 (1:200), and androgen receptor (1:50). The Dana-Farber Breast Cancer Tissue Microarray (TMA) consists of primary TNBC samples from approximately 83 patients who underwent definitive breast surgery at Brigham and Women's Hospital between 1 January 1997 and 31 December 2005. Formalin-fixed, paraffin-embedded breast cancers were collected from the archives of the Department of Pathology at Brigham and Women's Hospital. Best blocks and best areas for coring were identified and selected by a breast pathologist (DD) to represent different area of the tumour. Results of immunohistochemical studies for oestrogen (ER) and progesterone receptor (PR) and HER2 and FISH assay results for HER2 were extracted from pathology reports. TMA construction was carried out in the Dana-Farber/Harvard Cancer Center Tissue Microarray Core Facility. Three 0.6 mm cores were taken from different marked areas in each case and placed into a recipient block using a manual arrayer (Beecher Instruments). Specimens are arrayed in triplicate. Participants signed consent for research use of tissue and the linking of tumour specimens to clinical follow-up. Clinical data on these patients was collected retrospectively at first presentation, at 4, 9, 18, 30, and 42 months, and annually thereafter. After 9.3 years median follow up, 24 recurrences and 14 deaths have been recorded. The data elements are the following: staging, tumour pathology, diagnostic and follow-up tests performed, treatments administered (surgery, radiation and systemic therapy), and recurrence. Although the patients in this cohort were not treated as part of a clinical trial protocol, they were treated relatively uniformly as per Dana-Farber clinical practice guidelines. This serves to minimize confounding due to treatment heterogeneity. The TMA was stained with pBRD4 (1:200) antibody and imaged manually on Yokagawa spinning disc confocal microscope.

Three images were taken per each core for 240 out of 267 cores, for the remaining 27 one or two images were taken due to tissue loss or low tumour content. Image analysis was performed with ImageJ software macro (code available upon request). Phospho-BRD4 staining mean intensity was calculated per individual nucleus within an image. The mean intensity per image was normalized to nuclei count. For clinical outcome analysis patients were dichotomized as 'High'/'Low' pBRD4 by median intensity (Supplementary Table 9). Disease outcomes were evaluated in 83 of 89 TMA samples (3 were not TNBC by definitive pathology, 2 did not have clinical data available, one was a repeat biopsy on a patient). Recurrence-free survival (RFS) was defined as the interval from the date of initial surgical resection to the date of recurrence (local or distant), or date of last known contact if the patient was alive and has not recurred. RFS and overall survival were estimated using the Kaplan-Meier product-limit method, with hazard ratios and 95% confidence intervals from a univariate Cox proportional hazard model.

siRNAs and lentiviral shRNA and expression constructs. For siRNA transfection cells were plated at 2,000 cells per well in 96-well plates and cultured at 37 °C with 5% CO₂ in the media. The next day, cells were transfected in triplicate with siGENOME SMARTpools for the genes of interest or "Non-Targeting siRNA" controls using DharmaFECT 1 (Dharmacon). The sequences of the siRNAs in the SMARTpools are listed in Supplementary Table 10. Cell viability was measured using CellTiter-Glo (Promega) three days after transfections, with the effects of each siRNAs treatment on each cell line compared to the effects of no siRNAs.

TET-inducible pLKO-TET-ON lentiviral constructs were packaged by co-transfection of the lentiviral hairpin containing plasmid PLKO.1 and the helper plasmids pCMV-dR8.91 and pMD2.G-VS.V-G into HEK293T cells using Lipofectamine (Life Technologies). Following transduction via spinoculation for 30 min at 1,000g and selection with 1 µg ml⁻¹ puromycin for 72 h (Sigma, St. Louis, MO), knockdown efficacy was determined by western blotting and cells were seeded for proliferation assays as described above. Sequences of shRNAs used are listed in Supplementary Table 10.

Full length BRD4 in pCDNA3 was a gift from Dr. French at Brigham and Women's Hospital, Harvard Medical School. Mutations of BRD4 BD1 (N140A) and BD2 (N433A) bromodomains, 7A and 7D mutants were generated using a Quickchange Multi Site-Directed Mutagenesis Kit (Agilent Technologies) using primers listed in Supplementary Table 10 and subsequently verified by sequencing. **Immunoblotting and immunoprecipitation experiments.** Cells were lysed five days after transfection with siRNAs in RIPA buffer. Proteins were resolved in SDS-polyacrylamide gels (4–12%) and transferred to PVDF membranes by using a Tris-glycine buffer system. Membranes were blocked with 5% milk powder in 0.1% Tween20 in PBS (PBS-T) for 1 h at room temperature followed by incubation with primary antibodies at 1:1,000 dilution in 2.5% milk PBS-T. For immunoprecipitation, nuclear extracts were prepared as follow: 1 × 10⁷ cells were resuspended in 5 ml buffer A: 10 mM Tris pH 7.9, 1.5 mM MgCl₂, 10 mM KCl, 0.05% NP-40, 1 mM DTT, and protease and phosphatase inhibitors. Cells were incubated on ice for 15 min and gently vortexed every 5 min. After centrifugation at 2,000g for 5 min, pellets were suspended in 0.3 ml buffer B (20 mM Tris pH 7.9, 25% glycerol, 0.42 M NaCl, 1.5 mM MgCl₂, 1 mM KCl, 0.5% NP40, 0.2 mM EDTA, 1 mM DTT, and protease and phosphatase inhibitors) and incubated for 5 min on ice. After centrifugation of the lysates at 14,000g for 10 min at 4 °C, supernatant was diluted with 0.6 ml buffer A, and added NP-40 to final 0.5% and treated with DNase I. The samples were then incubated at 4 °C overnight with BRD4 or Flag antibodies at 1:100 dilution and immunoprecipitates were collected on Dynabeads Protein G for 2 h. Beads were washed with buffer B containing 150 mM NaCl and 0.5% NP-40 three times and then resuspended in gel loading buffer. Immunoblotting and immunoprecipitation experiments were repeated 2–3 times.

Antibodies and inhibitors. Antibodies used for immunoblotting, immunoprecipitation and ChIP-seq were as follows: BRD4 (Bethyl, A301-985A), MED1 (Bethyl, A300-793a), BRD3 (Bethyl, A302-368A), BRD2 (Bethyl, A302-583A), MYC (Santa Cruz, sc764), pSTAT3 (Cell Signaling, 9145S), STAT3 (Cell Signaling, 4904), pSTAT5 (Cell Signaling, 9351), pJAK2 (Cell Signaling, 3771), CYCLIN D1 (Cell Signaling, 2922), pH3 (Cell Signaling, 12201), CK2 substrate (Cell Signaling, 8738), PP2A-A (Cell Signaling, 2039), PP2A-C (Cell Signaling, 2038) and pBRD4 was a gift from C. M. Chiang. Antibodies used for ChIP-seq were BRD4 (Bethyl) histone H3K27ac (Abcam, ab4729), CXCR2 inhibitor (239819) and CK2 inhibitor (218860) were from CalBiochem, JAK2 inhibitor (Ruxolitinib, INCBO18424), MEK inhibitor (GSK1120212, S2673), ABT-737 (s1002), and PI3K inhibitor (BKM120, S2247) were from Selleckchem, phenothiazine (1525707) and perphenazine (1511000) were from Sigma-Aldrich. Inhibitor treatment for immunoblot analyses was conducted for 3 h.

SILAC-RIME experiments and data analysis. SUM159 and SUM159R cells were grown in R/K-deficient SILAC DMEM (paa; E15-086), 10% dialysed serum (Sigma-Aldrich; F0392), and supplemented with 800 µM L-lysine ¹³C₆¹⁵N₂

hydrochloride and 482 µM L-arginine ¹³C₆¹⁵N₂ hydrochloride (Cambridge Isotope laboratory) for 'heavy'-labelled media or 800 µM L-lysine ¹²C₆¹⁴N₂-hydrochloride and 482 µM L-arginine ¹²C₆¹⁴N₄ hydrochloride for 'light'-labelled media. After SILAC labelling, RIME was performed as described²⁰. Word clouds for Extended Data Fig. 7 were generated using R version 3.1.0 and the R package 'wordcloud' version 2.5. The size of the tag reflects the square root of the MASCOT score of the protein (the choice of square root is arbitrary, but visually appealing). Experiments were filtered against the Contaminant Repository for Affinity Purification Mass Spectrometry Data³⁰, considering any protein which occurs in at least 20 negative control experiments to be contamination, hence removed from the data set. Refseq protein IDs provided by the contaminant repository were converted to Uniprot IDs found in the mass spec experiments using mappings from the Bioconductor package 'org.Hs.eg.db', version 2.14 (Carlson M. org.Hs.eg.db: Genome wide annotation for Human. R package version 3.0.0). SILAC RIME experiments were performed in duplicates and repeated 2–3 times.

In vitro Chem-seq, ChIP-seq, and RNA-seq. Chem-seq was performed essentially as described¹¹. BRD4 ChIP-seq: SUM159 and SUM159R cells (4 × 10⁷) were grown in SUM Medium. The media were then removed and replaced with media containing 1% formaldehyde (EM grade; tebu-bio) and crosslinked for 8 min. Crosslinking was quenched by adding glycine to a final concentration of 0.2 M. The cells were washed with ice-cold PBS, harvested in PBS, and the cell pellet was washed with PBS. The nuclear fraction was extracted by first resuspending the pellet in 10 ml of LB1 buffer (50 mM HEPES-KOH (pH 7.5), 140 mM NaCl, 1 mM EDTA, 10% glycerol, 0.5% NP-40 or Igepal CA-630, and 0.25% Triton X-100) for 10 min at 4 °C. Cells were pelleted, resuspended in 10 ml of LB2 buffer (10 mM Tris-HCl (pH 8.0), 200 mM NaCl, 1 mM EDTA, and 0.5 mM EGTA), and mixed for 5 min. Cells were pelleted and resuspended in 300 µl of LB3 buffer (10 mM Tris-HCl (pH 8), 100 mM NaCl, 1 mM EDTA, 0.5 mM EGTA, 0.1% Na-deoxycholate, and 0.5% N-lauroylsarcosine) and sonicated in a Covaris sonicator for 10 min. A total of 30 µl of 10% Triton X-100 was added, and lysate was centrifuged for 10 min at 20,000 rcf to purify the debris. The supernatant was then incubated with 100 µl of Dynabeads Protein G (Life Technologies, 10003D) prebound with 20 µg BRD4 antibody (Bethyl, A301-985A), and immunoprecipitation (IP) was conducted overnight in the cold room. The beads were washed ten times in 1 ml of RIPA buffer and twice in 100 mM ammonium hydrogen carbonate (AMBIC) solution. DNA was eluted in elution buffer (50 mM Tris-HCl pH 8, 10 mM EDTA, and 1% SDS). Cross-links were reversed overnight at 65 °C. RNA and protein were digested with 0.2 mg ml⁻¹ RNase A for 2 h followed by 0.2 mg ml⁻¹ Proteinase K for 1 h. DNA was purified with phenol-chloroform extraction and ethanol precipitation. Libraries for Illumina sequencing were prepared following the Rubicon ThruPLEX-FD kit for 10–12 cycles.

RNA-seq: SUM159 and SUM159R were incubated in biological duplicates for 3, 12 and 24 h with 500 nM of JQ1 or DMSO treatment. Total RNA was extracted using the standard Qiagen RNeasy kit (74106). RNA concentrations were measured and quality controlled on a Bioanalyzer, RNA-Seq libraries were made using Illumina True-Seq RNA kits using the Scicleone NGSe workstation.

All RNA-seq and ChIP-seq experiments were performed in duplicates.

Genomic data analyses. Accessing data generated in this manuscript. All ChIP-seq, Chem-seq, and RNA-seq data generated in this publication can be found online associated with GEO Publication Reference ID GSE63584 (www.ncbi.nlm.nih.gov/geo/). Supplementary Table 2 lists all sequencing data sets and their corresponding GEO GSM accession IDs.

Gene sets and annotations. All analysis was performed using RefSeq (NCBI37/HG19) human gene annotations.

RNA-seq data processing and gene expression quantification. All RNA-Seq data sets were aligned to the transcriptome using Tophat2³¹ (version 2.0.11) using the Illumina genomes NCBI37/HG19 UCSC transcriptome build retrieved from <http://ccb.jhu.edu/software/tophat/igenomes.shtml>. Alignments were performed using default parameters. Transcript expression quantification was performed using Cufflinks³² (version 2.2.0) with default parameters to generate gene expression values in units of FPKM.

ChIP-seq and Chem-seq data processing. All ChIP-seq and Chem-seq data sets were aligned using Bowtie2³³ (version 2.2.1) to build version NCBI37/HG19 of the human genome or build version NCB37/MM9 of the mouse genome. Alignments were performed using the following criteria: -k 1, with all other parameters set to default. These criteria preserved only reads that mapped uniquely to the genome without any mismatches.

Calculating read density. We calculated the normalized read density of a ChIP-seq or Chem-seq data set in any region using the Bamliquidator (version 0.9) read density calculator (<https://github.com/BradnerLab/pipeline/wiki/bamliquidator>). Briefly, ChIP-Seq reads aligning to the region were extended by 200 bp and the density of reads per base pair (bp) was calculated. The density of reads in each region was normalized to the total number of million mapped

reads producing read density in units of reads per million mapped reads per bp (rpm per bp).

Identifying ChIP-seq and Chem-seq enriched regions. We used the MACS version 1.4.2 (Model based analysis of ChIP-Seq)³⁴ peak finding algorithm to identify regions of ChIP-Seq enrichment over background. A *P* value threshold of enrichment of 1×10^{-9} was used for all data sets. The GEO accession number and background used for each data set can be found in the accompanying Supplementary Table 2.

Creating heat map representations of ChIP-seq occupancy. Heat maps of ChIP-seq occupancy for various factors were created as described³⁵. Heat maps were created for the ± 10 kb region flanking all transcription start sites (TSS) or for the ± 10 kb region flanking all TSS distal BET bromodomain bound enhancers. Each row plots a specific TSS or enhancer region. Rows are ranked by peak occupancy of BET bromodomains as determined by Bio-JQ1 Chem-seq signal (Fig. 1d).

Correlating BRD4 and H3K27ac occupancy to Bio-JQ1. Occupancy of BRD4 and H3K27ac was correlated to Bio-JQ1 occupancy at all regions of Bio-JQ1 enrichment in SUM159 cells. Pearson correlation statistics are shown (Extended Data Fig. 3a). To quantify changes in BRD4 or H3K27ac occupancy upon JQ1 treatment, all Bio-JQ1 enriched regions were ranked in SUM159 cells and then binned ($n = 10$). Corresponding box plots of BRD4 or H3K27ac \log_2 fold change with or without JQ1 are shown for each bin (Extended Data Fig. 3b).

Mapping enhancers and super-enhancers using Bio-JQ1 occupancy or BRD4. Enhancers and super enhancers (SEs) were mapped using the ROSE software package described^{12,13} and available at (http://younglab.wi.mit.edu/super_enhancer_code.html). In SUM159 and SUM159R cells, Bio-JQ1 Chem-Seq enriched regions were used to map enhancers and super enhancers (Fig. 1f). In SUM149 cells, BRD4 ChIP-seq enriched regions were used to map enhancers and super enhancers (Extended Data Fig. 3a). Enhancers are defined as regions of Bio-JQ1 binding not contained in promoters.

Quantifying changes in gene expression of super enhancer proximal genes. Genes within 50 kb of super enhancer in SUM159 or SUM149 were identified and filtered for expression status (>1 FPKM expression in any sample), and filtered to remove non poly-adenylated transcripts (for example, microRNAs). For SUM159, \log_2 fold changes in gene expression at super-enhancer-associated genes or all expressed genes was compared at 3, 12, and 24 h post JQ1 treatment (Fig. 1g). For SUM149, comparisons were made at 12 h post JQ1 treatment (Extended Data Fig. 3f). The statistical significance of differences between distributions of changes was also assessed using a Welch's two-tailed *t* test.

Identifying differentially expressed genes upon JQ1 treatment. To identify genes differentially regulated by JQ1 treatment in SUM159 or SUM149 cells, all genes with a >1 \log_2 fold change in expression were ordered by fold change at 24 h with or without JQ1 for SUM159 or at 12 h with or without JQ1 for SUM149. The \log_2 row median normalized fold change for each gene is displayed as a heat map in Extended Data Fig. 3g for SUM159 and in Extended Data Fig. 3h for SUM149. For subsequent gene set and pathway analysis, SUM159 genes with consistent and statistically significantly altered expression were selected using a Welch's two-tailed *t* test between DMSO and JQ1 treated expression values at 12 and 24 h. A *P* value cut-off of 0.01 was applied (Extended Data Fig. 3k).

Identifying gained/lost super enhancers between SUM159 and SUM159R. Super enhancer differential regions were defined as in Brown *et al.* 2014³⁶. Briefly, in order to quantify changes in super-enhancers between two conditions, background subtracted ChIP-Seq signal was calculated at the set of all enhancer regions considered super in at least one condition. Gained/lost super-enhancers were determined as those with a greater than \log_2 fold change signal in either direction. The \log_2 fold change in Bio-JQ1 occupancy at all rank ordered super-enhancer-containing regions is shown in Fig. 2c. Super enhancer regions were classified as either gained, conserved, or lost. Gained/lost regions were classified as those with >1 \log_2 fold change in either direction. Conserved regions were classified as those with <0.25 \log_2 fold change in either direction. The \log_2 fold change in either BRD4 or proximal (within 50 kb of region) gene expression is shown in Extended Data Fig. 5d-f.

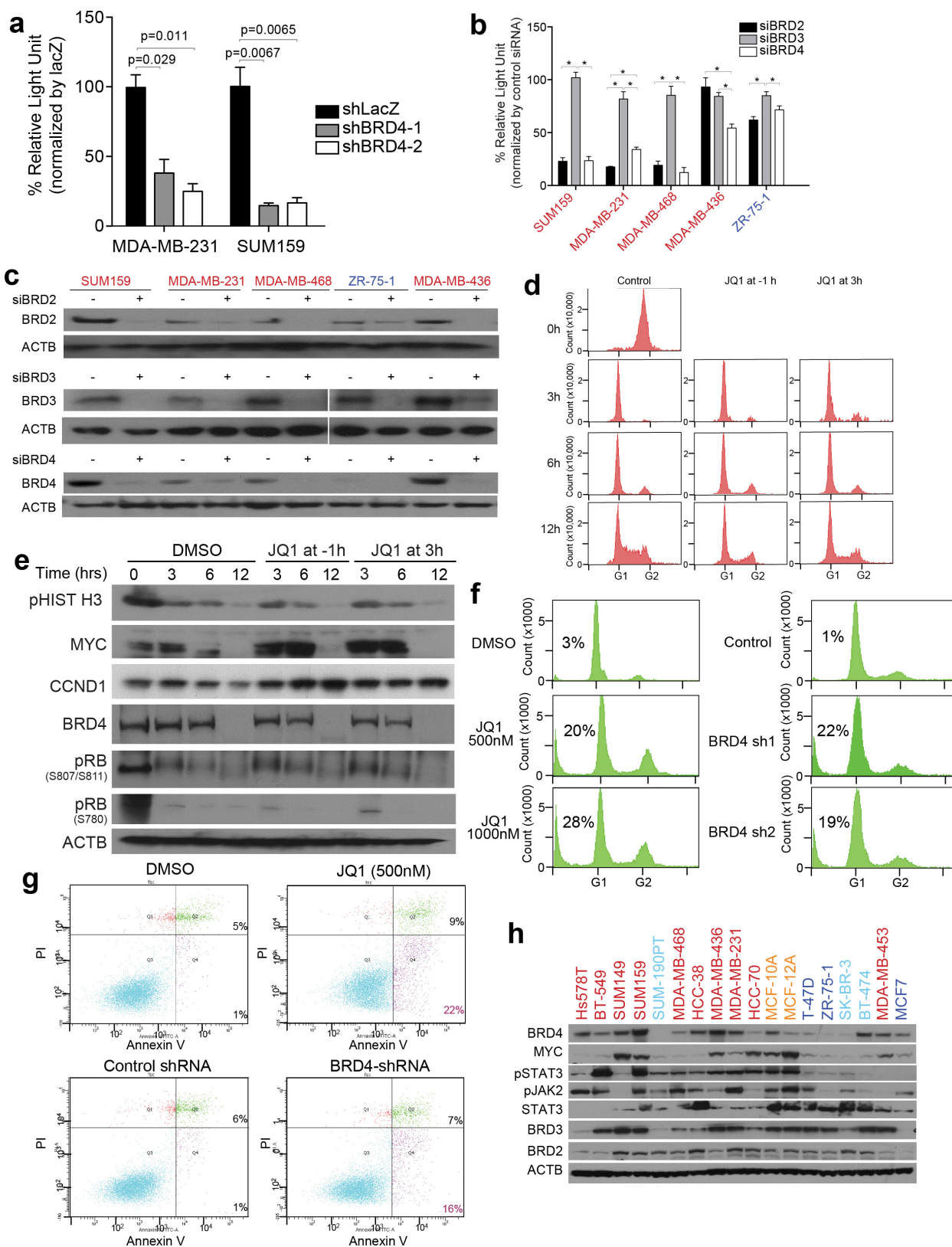
Quantifying changes in BRD4 and H3K27ac occupancy upon JQ1 treatment in either SUM159 or SUM159R cells at Bio-JQ1 regions. \log_2 fold changes in BRD4 or H3K27ac were quantified at Bio-JQ1 enriched regions in their respective cell line and shown in Extended Data Fig. 5c.

Quantifying changes in BRD4 and H3K27ac as a function of Bio-JQ1 or BRD4 occupancy. Bio-JQ1 enriched regions in SUM159 or BRD4 enriched regions in SUM149 were ranked by increasing levels and then distributed into 10 bins. \log_2 fold changes in BRD4 or H3K27ac were quantified in each bin of regions and displayed as a box plot (Extended Data Fig. 3b, c).

Quantifying changes in BRD4 occupancy upon JQ1 treatment in all TNBC. \log_2 fold changes in BRD4 upon JQ1 treatment were quantified at BRD4 enriched regions in each respective cell line Extended Data Fig. 6c.

All code related to genomic and transcriptome analysis can be found at <https://github.com/BradnerLab/TNBC>.

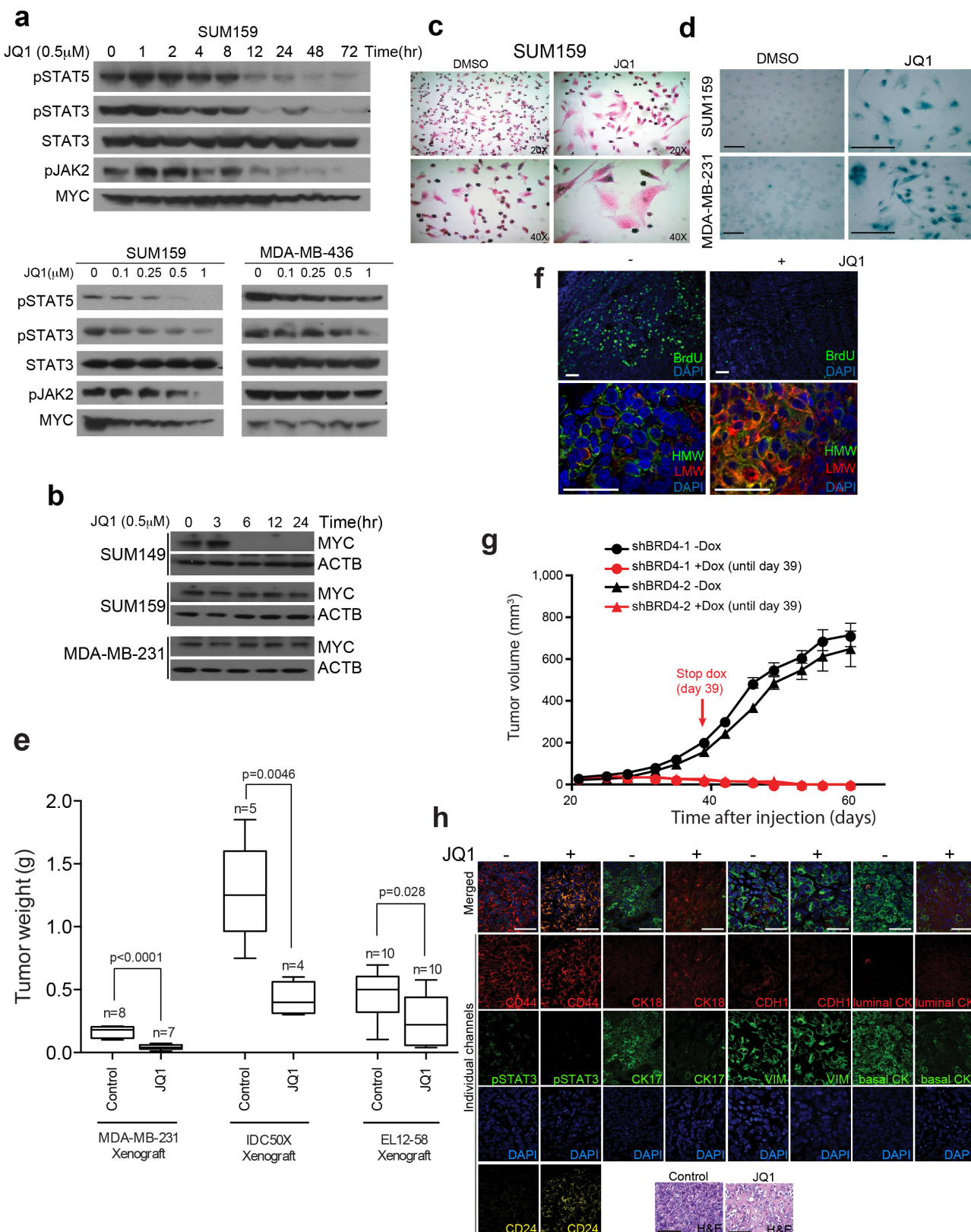
28. Chou, T. C. & Talalay, P. Quantitative analysis of dose-effect relationships: the combined effects of multiple drugs or enzyme inhibitors. *Adv. Enzyme Regul.* **22**, 27–55 (1984).
29. Choudhury, S. *et al.* Molecular profiling of human mammary gland links breast cancer risk to a p27⁺ cell population with progenitor characteristics. *Cell Stem Cell* **13**, 117–130 (2013).
30. Mellacheruvu, D. *et al.* The CRAPome: a contaminant repository for affinity purification-mass spectrometry data. *Nature Methods* **10**, 730–736 (2013).
31. Trapnell, C., Pachter, L. & Salzberg, S. L. TopHat: discovering splice junctions with RNA-Seq. *Bioinformatics* **25**, 1105–1111 (2009).
32. Trapnell, C. *et al.* Transcript assembly and quantification by RNA-Seq reveals unannotated transcripts and isoform switching during cell differentiation. *Nature Biotechnol.* **28**, 511–515 (2010).
33. Langmead, B., Trapnell, C., Pop, M. & Salzberg, S. L. Ultrafast and memory-efficient alignment of short DNA sequences to the human genome. *Genome Biol.* **10**, R25 (2009).
34. Zhang, Y. *et al.* Model-based analysis of ChIP-Seq (MACS). *Genome Biol.* **9**, R137 (2008).
35. Lin, C. Y. *et al.* Transcriptional amplification in tumor cells with elevated c-Myc. *Cell* **151**, 56–67 (2012).
36. Brown, J. D. *et al.* NF-κB directs dynamic super enhancer formation in inflammation and atherosclerosis. *Mol. Cell* **56**, 219–231 (2014).



Extended Data Figure 1 | See next page for figure caption.

Extended Data Figure 1 | BET bromodomain proteins and cell growth in TNBCs. All error bars represent s.d., $n = 3$. **a**, Cellular viability of SUM159 and MDA-MB-231 cells expressing TET-inducible BRD4-targeting or lacZ shRNAs. P values indicate statistical significance of the observed differences (paired t -test). **b**, Cellular viability four days after transfection of siRNAs targeting BET bromodomain proteins. Asterisks indicate statistical significance (paired t -test) of the marked differences as follows. SUM159: siBRD2 versus siBRD3, $P = 0.002$; siBRD3 versus siBRD4, $P = 0.0006$, MDA-MB-231: siBRD2 versus siBRD3, $P = 0.006$; siBRD2 versus siBRD4, $P = 0.002$; siBRD3 versus siBRD4, $P = 0.016$, MDA-MB-468: siBRD2 versus siBRD3, $P = 0.0009$; siBRD3 versus siBRD4, $P = 0.0055$, MDA-MB-436: siBRD2 versus siBRD4, $P = 0.002$; siBRD3 versus siBRD4, $P = 0.015$, ZR-75-1: siBRD2 versus siBRD3, $P = 0.0169$; siBRD3 versus siBRD4, $P = 0.007$. **c**, Immunoblot analysis of BET bromodomain proteins four days after siRNA transfection.

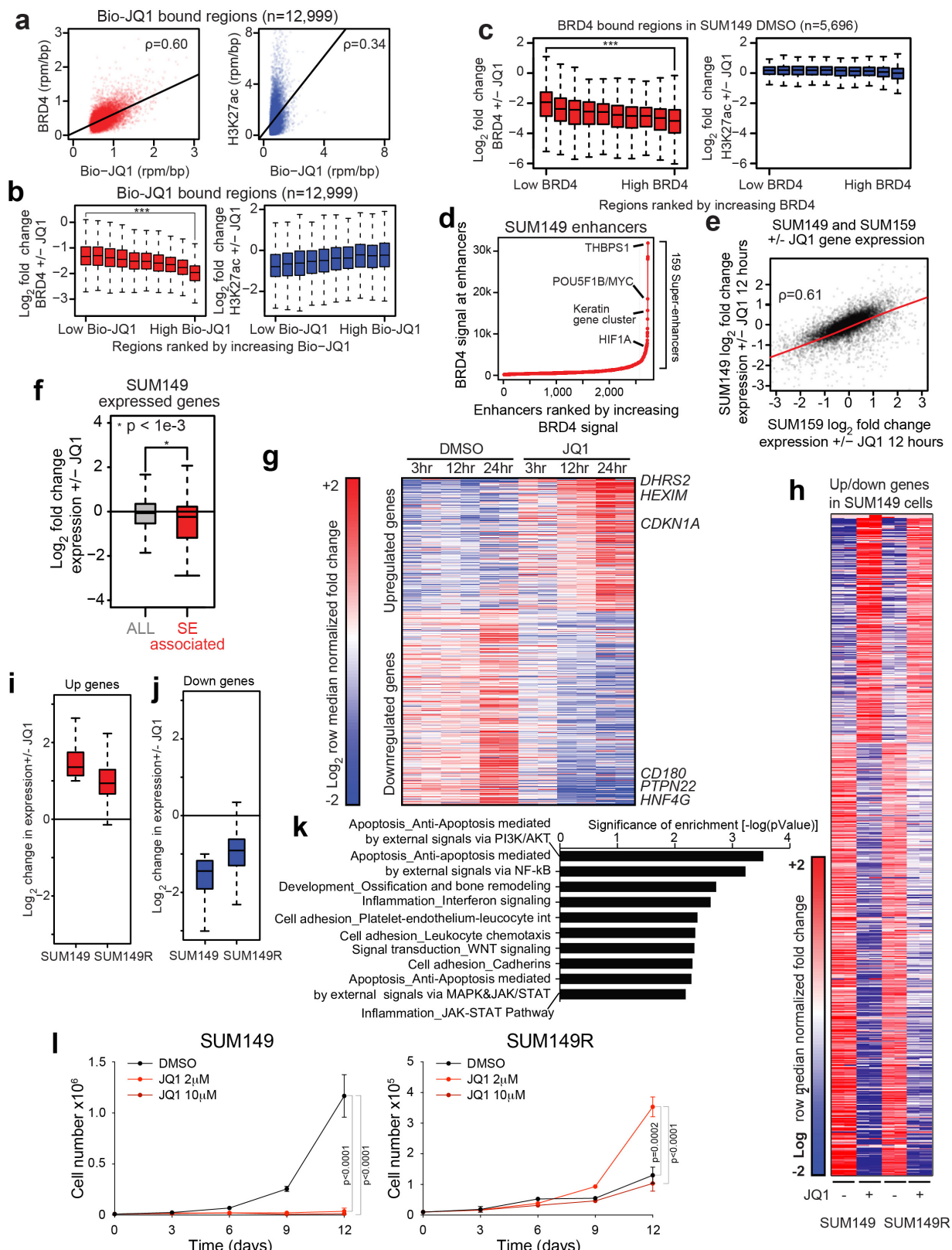
d, Cell cycle profile of SUM159 cells synchronized in G2/M with 100 ng ml $^{-1}$ nocodazole followed by replating to fresh medium with DMSO or JQ1 (500 nM) added at -1 h or at 3 h after release. Cells were collected at different time points (0, 6, 12 h) after release. **e**, Immunoblot analysis of the indicated proteins at different time points (0, 3, 6, 12 h) after release of SUM159 cells synchronized with 100 ng ml $^{-1}$ nocodazole followed by replating to fresh medium with DMSO or JQ1 (500 nM) added at 1 h before or 3 h after release. **f**, Cell cycle analysis of SUM159 cells following 72 h treatment with JQ1 (500 nM) or downregulation of BRD4 using TET-inducible shRNAs. **g**, Annexin V staining of SUM159 cells following 72 h treatment with JQ1 (500 nM) downregulation of BRD4 using TET-inducible shRNAs. All error bars represent s.e.m. **h**, Immunoblot analysis of the indicated proteins in a panel of breast cell lines; colour scheme as in **a**. For gel source data, see Supplementary Fig. 1.



Extended Data Figure 2 | See next page for figure caption.

Extended Data Figure 2 | Response to BBIs in TNBCs. **a**, Immunoblot analysis of the indicated proteins at different time points following JQ1 treatment (500 nM) in SUM159 cells (top) and at different JQ1 doses for 24 h treatment in SUM159 and MDA-MB-436 cells (bottom). **b**, Immunoblot analysis of the indicated proteins at different time points following JQ1 treatment (500 nM) in SUM149, SUM159 and MDA-MB-231 cells. **c**, Haematoxylin and eosin staining of SUM159 cells after 3 days of JQ1 treatment. **d**, Senescence β -galactosidase staining of SUM159 and MDA-MB-231 cells after 3 days of JQ1 treatment. Scale bars, 100 μ m. **e**, Box plots depict the weights of xenografts 30 days after injection of MDA-MB-231 (2×10^6) and IDC50X (2×10^5) cells into inguinal mammary fat pads of NOG mice; n indicates the number of mice per experiment. P values indicate statistical significance of the observed differences (unpaired t -test). Error bars represent s.e.m. Mice were administered JQ1 (50 mg per kg, daily) or vehicle only (control) for 14 days beginning at day 16 (MDA-MB-231) or 10 (IDC50X) after injection (after tumours reached palpable size). For EL12-58X PDX, mice were

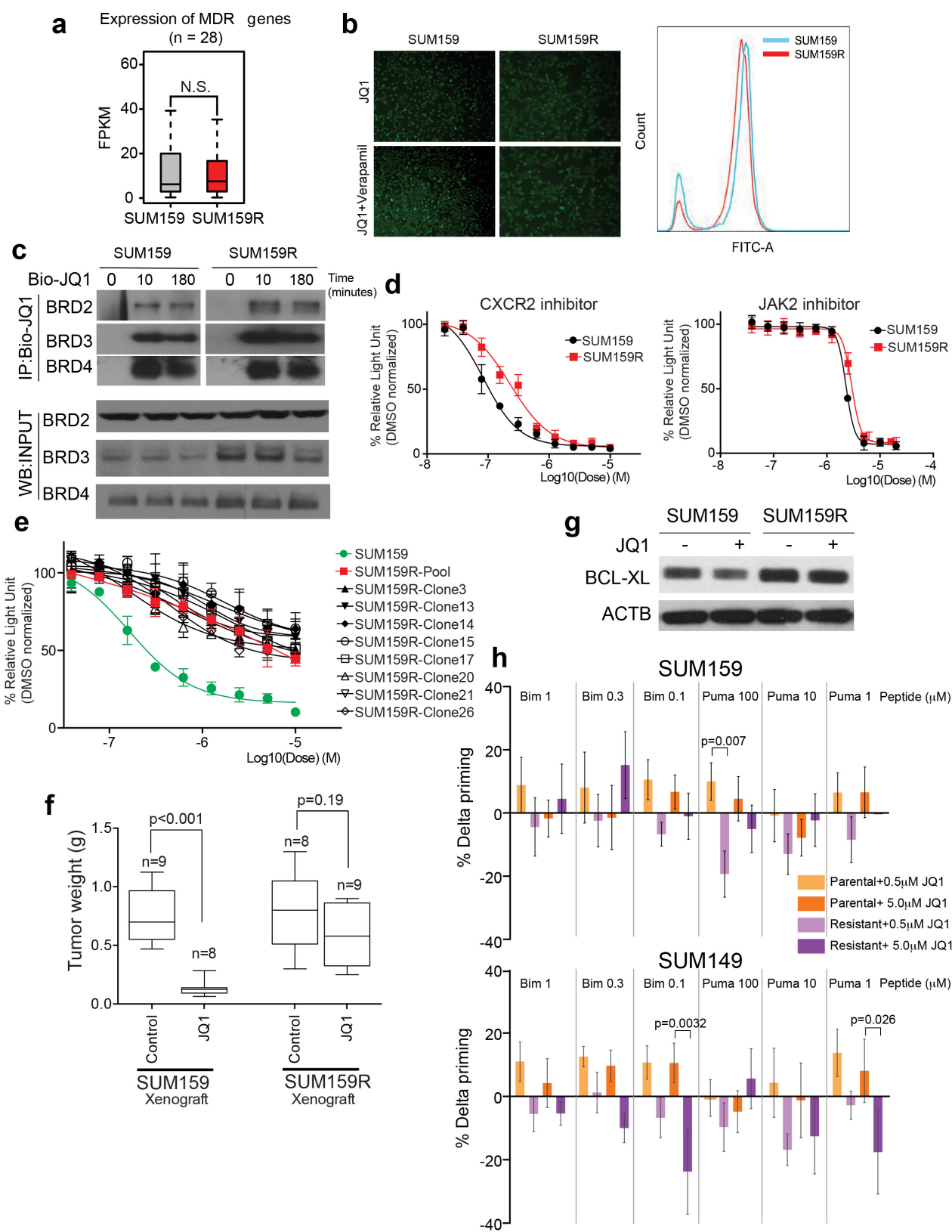
implanted with pieces of tissue measuring $1 \times 3 \times 3$ mm into the inguinal mammary fat pads and were administered daily JQ1 (50 mg per kg) for 14 days beginning at day 21 after injection (after tumours reached palpable size). **f**, Bromodeoxyuridine (BrdU) and luminal (Low MW CK) and basal high (High MW CK) molecular weight cytokeratin staining of EL12-58 xenograft with or without JQ1 treatment. Scale bars, 50 μ m. **g**, Tumour volume of SUM159 cells expressing TET-inducible BRD4-targeting shRNAs. Mice were administered doxycycline or vehicle only (control) for 39 days beginning at day 21 after injection (after tumours reached palpable size). Error bars represent s.d., $n = 4$ (shBRD4-1 experiment) and $n = 5$ (shBRD4-2 experiment). **h**, Haematoxylin and eosin staining and immunofluorescence analysis of basal (basal cytokeratin, cytokeratin 17, pSTAT3, and CD44) and luminal (luminal cytokeratin, cytokeratin 18, and CD24) markers in SUM159 xenografts with or without JQ1 treatment. Scale bars, 100 μ m for haematoxylin and eosin and 50 μ m for immunofluorescence, respectively. For gel source data, see Supplementary Fig. 1.



Extended Data Figure 3 | See next page for figure caption.

Extended Data Figure 3 | SUM149 JQ1 response. **a**, Scatter plots showing the relationship between the genomic binding of BRD4 and Bio-JQ1 (left) or H3K27ac and Bio-JQ1 (right) at all Bio-JQ1 enriched bound regions. Units of genomic occupancy are in rpm per bp. A simple linear regression is drawn in black. Pearson correlation statistics are also shown. **b**, Box plots showing the \log_2 fold change in BRD4 with or without JQ1 (left) or H3K27ac with or without JQ1 (right) at Bio-JQ1 bound regions in SUM159 cells. The 12,999 Bio-JQ1 regions are ranked by increasing Bio-JQ1 binding and divided into 10 separate bins (displayed from left to right). The statistical significance of the difference in the mean BRD4 \log_2 fold change between the weakest and strongest Bio-JQ1 bound region bins is shown (Welch's *t*-test; ****P* value $< 1 \times 10^{-10}$). **c**, Box plots showing the \log_2 fold change in BRD4 with or without JQ1 (left) or H3K27ac with or without JQ1 (right) at BRD4 bound regions in SUM149 cells. The 5,696 BRD4 bound regions are ranked by increasing background subtracted BRD4 binding and divided into 10 separate bins (displayed from left to right). The statistical significance of the difference in the mean BRD4 \log_2 fold change between the weakest and strongest BRD4 bound region bins is shown (Welch's *t*-test; ****P* value $< 1 \times 10^{-10}$). **d**, Ranked plots of enhancers defined in untreated SUM149 cells ranked by increasing BRD4 signal (units rpm). Enhancers are defined as regions of BRD4 binding not contained in promoters. The cut-off discriminating typical from super-enhancers is shown as a dashed grey line. Enhancers associated with TNBC characteristic genes are highlighted. **e**, Scatter plots showing the relationship between the \log_2 fold change in gene expression upon 12 h JQ1 treatment in SUM149 (*y*-axis) and SUM159 (*x*-axis) cells. A simple linear regression is drawn in red. The Pearson

correlation statistic is also shown. **f**, Box plots showing the \log_2 fold change in expression relative to DMSO control of either all active genes or super-enhancer (SE)-associated genes upon 12 h JQ1 treatment. The statistical significance of the difference in expression change between all active genes and super-enhancer-associated genes is shown by a Welch's *t*-test **P* value $< 1 \times 10^{-3}$. **g**, Heat map showing the expression of genes that are up or down regulated by JQ1 versus DMSO after 24 h treatment. Each row shows the expression of a single gene in either DMSO or JQ1 treated cells at 3, 12, and 24 h after treatment. Expression values are coloured according to fold change relative to the median for each row. Genes are ordered by fold change with or without JQ1 24 h after treatment. **h**, Heat map showing the expression of genes that are up or down regulated by JQ1 versus DMSO after 12 h treatment in SUM149 and SUM149R cells. Each row shows the expression of a single gene in either DMSO or JQ1 treated cells at 12 h after treatment. Expression values are coloured according to fold change relative to the median for each row. Genes are ordered by fold change with or without JQ1 12 h after treatment in SUM149 cells. **i, j**, Box plots showing the \log_2 fold change in expression at genes that are up- (**i**) or down- (**j**) regulated by JQ1 versus DMSO after 12 h of treatment in parental SUM149 cells. Log₂ fold change in expression is shown for either parental SUM149 (left) or resistant SUM149R (right) cells. **k**, Top signalling pathways affected by JQ1-induced gene expression changes in SUM159 cells. **l**, Viable cell numbers of SUM149 (left) and SUM149R (right) cells treated with different doses of JQ1 (2 μ M, 10 μ M). Error bars represent s.d., *n* = 3. *P* values indicate statistical significance of the observed differences (two-way ANOVA with Bonferroni multiple comparison correction).

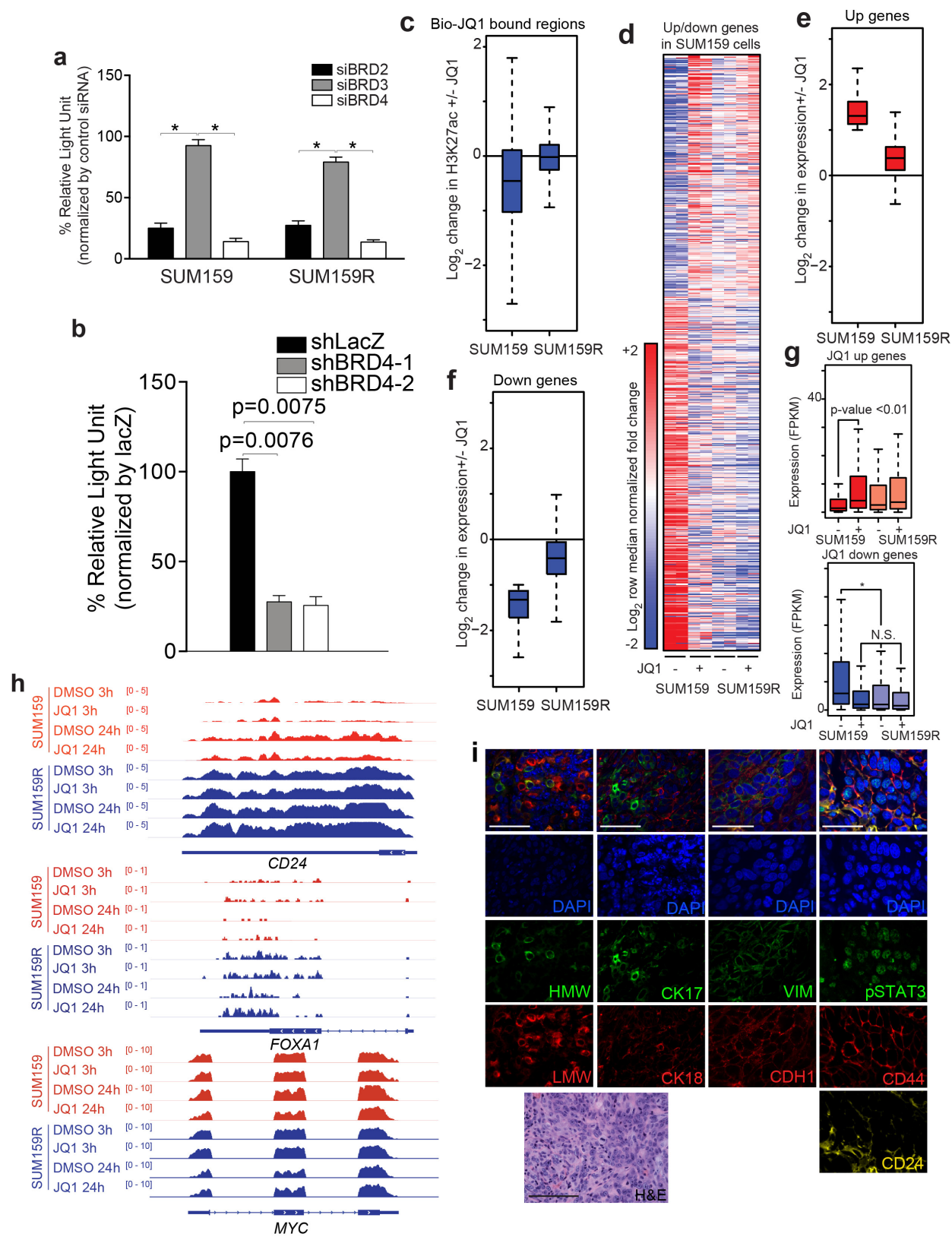


Extended Data Figure 4 | See next page for figure caption.

Extended Data Figure 4 | Characterization of SUM159R cells.

a, Expression of ABC transporters in SUM159 and SUM159R cells. The expression of 29 ABC transporters was analysed based on RNA-seq data on the two cell lines. **b**, Assay for MDR (multi drug resistance) pumps in SUM159 and SUM159R cells treated with JQ1 alone or together with verapamil based on microscopic examination (left) and FACS (right) of cells labelled with fluorescent MDR substrate. **c**, Immunoprecipitation analysis of Biotinylated JQ1 (Bio-JQ1) in SUM159 and SUM159R cells with JQ1 treatment at different time points following immunoblot for the indicated proteins. **d**, Cellular viability of SUM159 and SUM159R cells treated with CXCR2 and JAK2 inhibitors. Error bars represent s.d., $n = 3$. **e**, Cellular viability of SUM159, and pool and single cell clones of SUM159R cells treated with different doses of JQ1. Error bars represent s.d., $n = 3$. **f**, Tumour weight of xenografts derived from SUM159 and

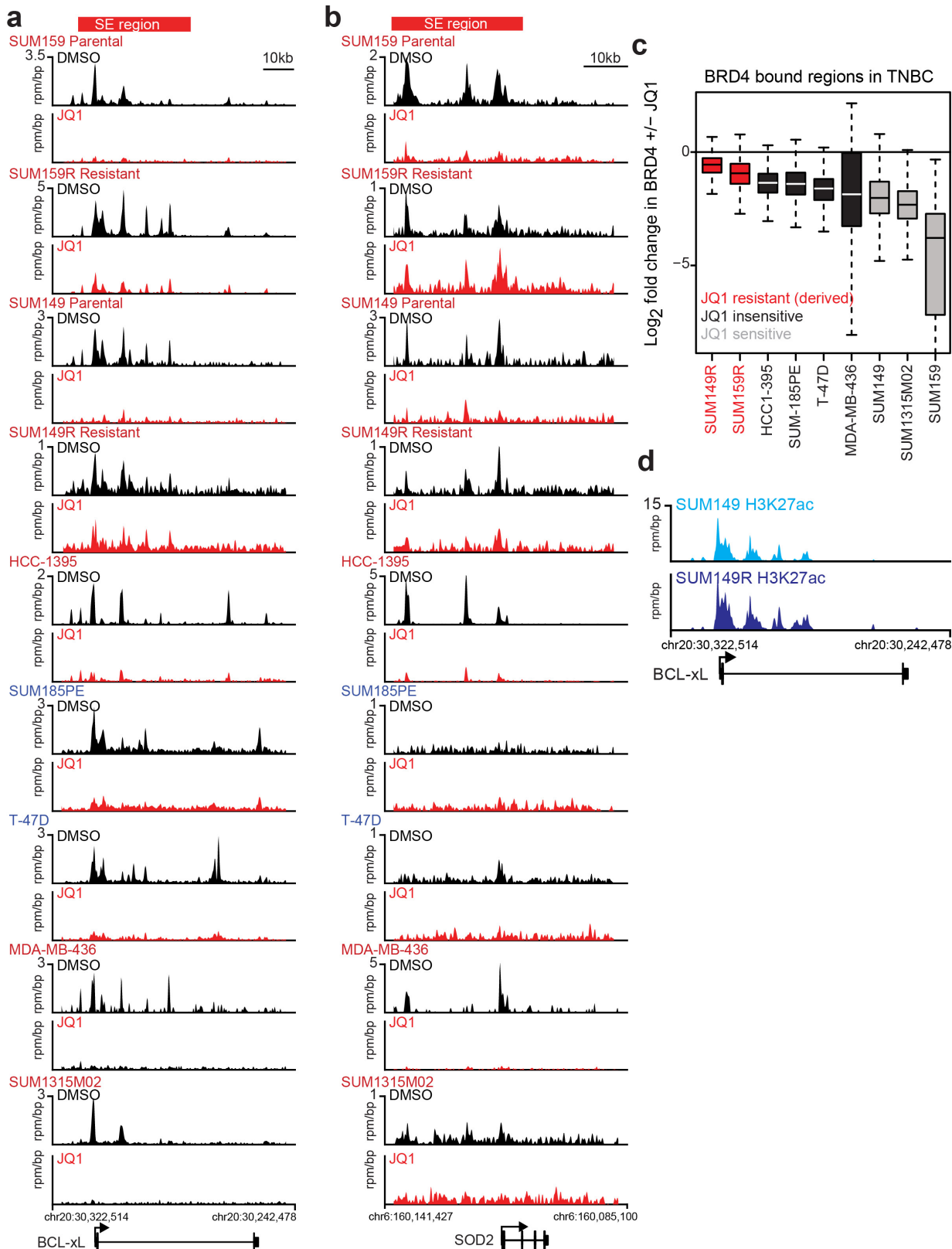
SUM159R cells. Mice were administered JQ1 for 14 (SUM159) and 30 (SUM159R) days beginning at day 14 and 26, respectively, after injection. P values indicate statistical significance of the observed differences (unpaired t -test). Error bars represent s.e.m. **g**, Immunoblot analysis of BCL-XL expression in SUM159 and SUM159R cells before and after JQ1 3 h treatment (500 nM). **h**, Dynamic BH3 profiling reveals inverse apoptotic response to JQ1 in SUM149R and SUM159R cells. In parental lines JQ1 increases priming relative to untreated cells indicating an increase in apoptotic propensity. In resistant lines JQ1 reduces priming indicating greater resistance to apoptosis relative to untreated cells. P values indicate statistical significance of the observed differences (two-way ANOVA). Error bars represent s.e.m., $n = 5$. For gel source data, see Supplementary Fig. 1.



Extended Data Figure 5 | See next page for figure caption.

Extended Data Figure 5 | BRD4 binding in SUM159R cells. **a**, Cellular viability of SUM159 and SUM159R cells transfected with siRNAs targeting bromodomain proteins. Asterisks indicate statistical significance (paired *t*-test) of the marked differences as follows: SUM159: siBRD2 versus siBRD3, $P = 0.013$, siBRD3 versus siBRD4, $P = 0.0154$ and SUM159R: siBRD2 versus siBRD3, $P = 0.0159$, siBRD2 versus siBRD4, $P = 0.0048$; siBRD3 versus siBRD4, $P = 0.0068$. **b**, Cellular viability of SUM159R cells expressing TET-inducible BRD4-targeting or lacZ shRNAs. All error bars represent s.e.m. *P* values indicate statistical significance of the observed differences (unpaired *t*-test). **c**, Box plot showing the log₂ fold change in H3K27ac genomic occupancy at regions bound by Bio-JQ1 in parental SUM159 or resistant SUM159R cells. **d**, Heat map showing the expression of genes that are up or down regulated by JQ1 versus DMSO after 24 h treatment in parental SUM159 cells. Each row shows the expression of a single gene in either DMSO or JQ1 treated cells at 24 h after treatment in SUM159 cells (left four columns) or SUM159R cells (right four columns). Expression values are coloured according to fold change relative to the median for each row. Genes are ordered by fold change with or without JQ1 24 h after treatment. **e, f**, Box plots showing the log₂ fold change in expression at genes that are up- (**e**) or down- (**f**) regulated by JQ1

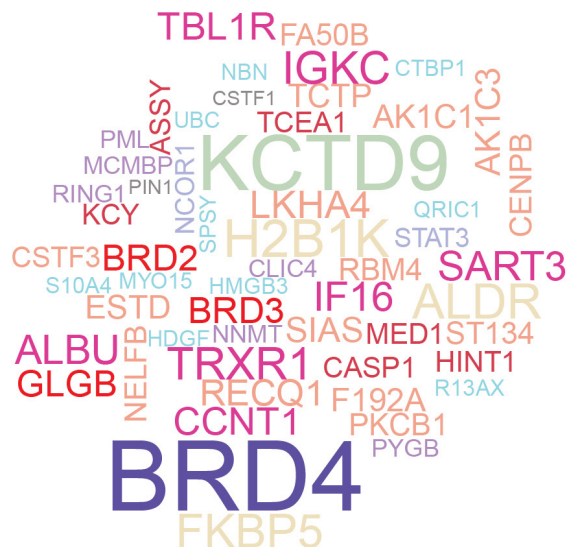
versus DMSO after 24 h of treatment in parental SUM159 cells. Log₂ fold change in expression is shown for either parental SUM159 or resistant SUM159R cells. **g**, Box plots showing expression of genes that are up- or downregulated by JQ1 versus DMSO after 24 h of treatment in parental SUM159 cells. Expression is shown in DMSO and JQ1-treated conditions in units of FPKM for either parental SUM159 (left) or resistant SUM159R (right) cells. The statistical significance of the difference between gene expression distributions for SUM159 DMSO- and JQ1-treated cells is shown ($P < 0.01$). The difference between all other distributions are considered non significant (NS). The statistical significance of the difference between SUM159 DMSO gene expression distribution and all other distributions is shown (* $P < 1 \times 10^{-3}$). The difference between all other distributions are considered non-significant. **h**, Examples of luminal and basal cell-specific genes, and MYC in SUM159 and SUM159R cells. RNA-seq tracks are shown. **i**, Haematoxylin and eosin staining and immunofluorescence analysis of luminal (CK18 and LMW) and basal (CK17 and HMW) cytokeratins and luminal (VIM and CD24) and basal (CDH1, CD44, and pSTAT3) cell markers in SUM159R xenografts. All error bars represent s.e.m. Scale bars, 100 μ m for haematoxylin and eosin and 50 μ m for immunofluorescence, respectively.



Extended Data Figure 6 | JQ1 response in other breast cancer cell lines. **a, b**, Gene tracks depicting BRD4 + DMSO and BRD4 + JQ1 in multiple breast cancer cells at the *BCL-XL* (a) or *SOD2* (b) gene loci. The x-axis shows position along the chromosome with gene structures drawn below. The y-axis shows genomic occupancy in units of rpm per bp. The *BCL-XL* and *SOD2* super-enhancers are shown as a red bar at the top. **c**, Box plots showing the log₂ fold change in BRD4 occupancy with or without JQ1 for

all BRD4 bound regions in each cell line for multiple TNBC. Cell lines are ordered by their JQ1 (IC_{50}) and coloured by their sensitivity. **d**, Gene tracks depicting H3K27AC occupancy at the *BCL-xL* locus in SUM149 parental (top, light blue) or SUM149R resistant (bottom, dark blue) cells. The x-axis shows position along the chromosome with gene structures drawn below. The y-axis shows genomic occupancy in units of rpm per bp. All error bars represent s.e.m.

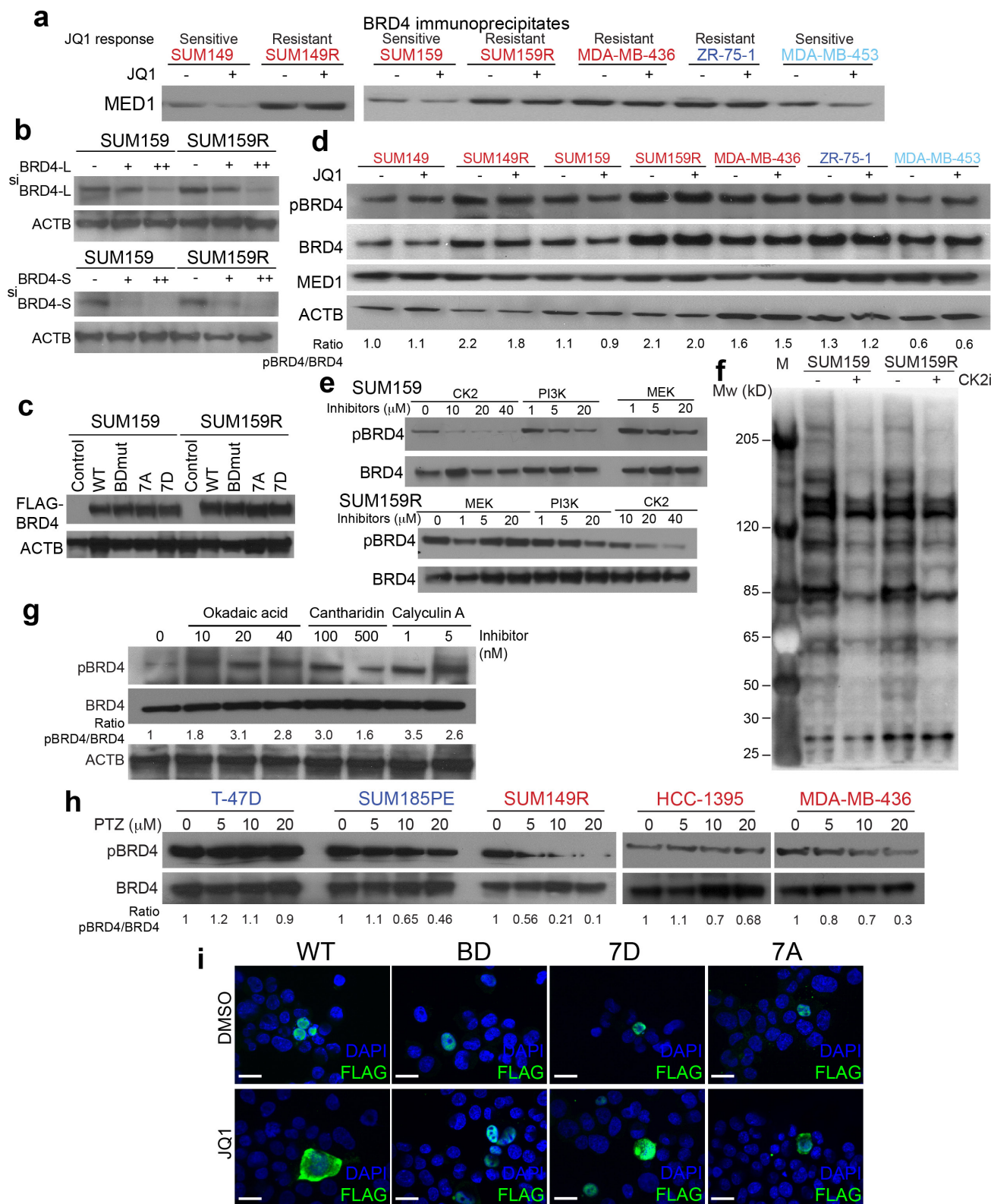
SUM159



SUM159R

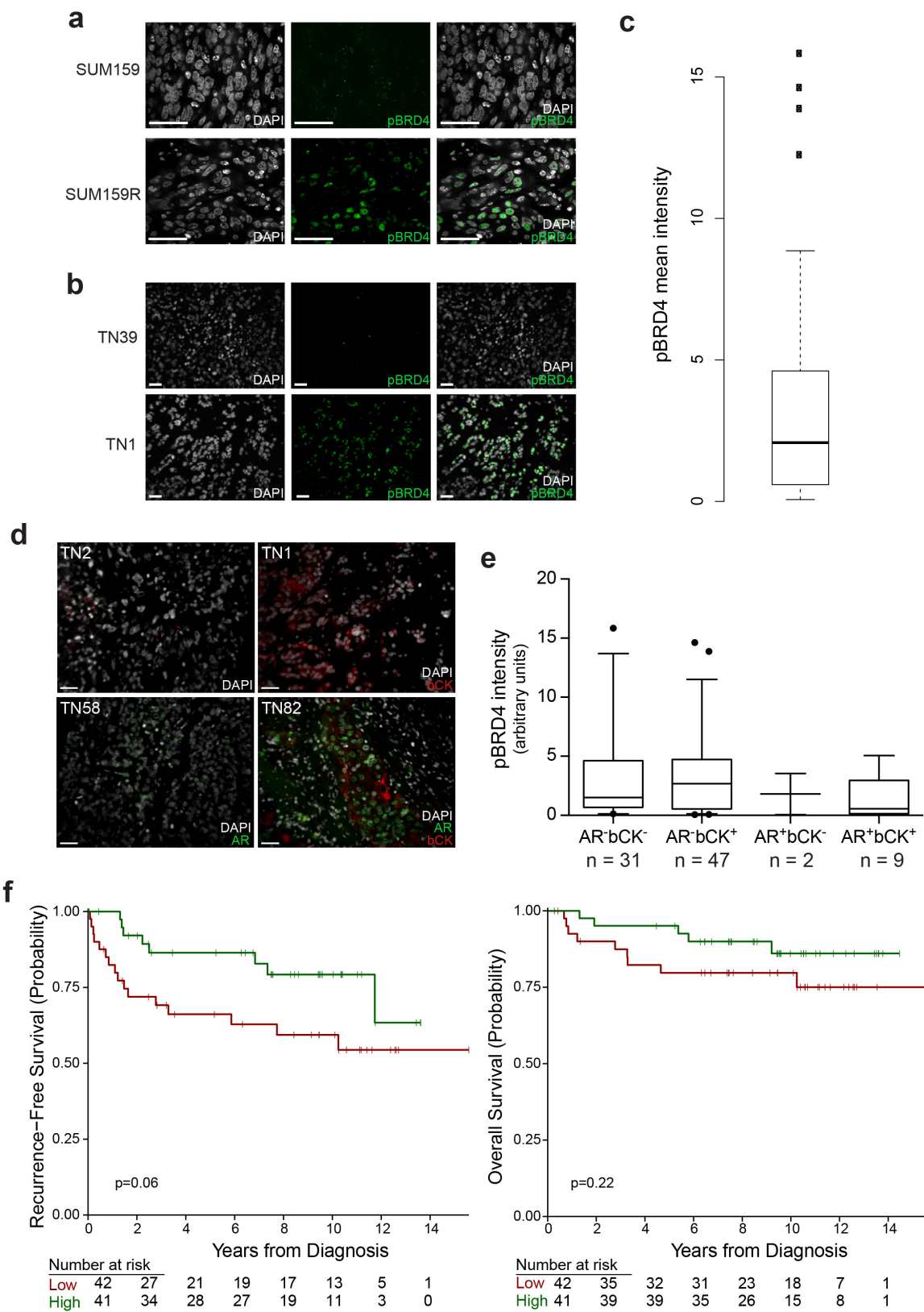


Extended Data Figure 7 | Word clouds depicting BRD4-associated proteins identified in RIME analysis.



Extended Data Figure 8 | Mechanism of BBI-resistance. **a**, Immunoblot analysis of BRD4 immunoprecipitates for MED1 in the indicated cell lines with or without JQ1 treatment (5 μ M, 3 h). **b**, Immunoblot analysis of long (BRD4L) and short (BRD4S) forms of BRD4 after transfection of siRNAs. **c**, Immunoblot analysis of the indicated exogenously expressed Flag-tagged BRD4 proteins in SUM159 and SUM159R cells. **d**, Immunoblot analysis of pBRD4, BRD4, MED1 and ACTB in the indicated cell lines with or without JQ1 treatment. **e**, Immunoblot analysis of phospho-BRD4 (pBRD4) and BRD4 in SUM159 and SUM159R cells treated with the indicated doses of CK2, PI3K, and MEK inhibitors for 2 h. **f**, Immunoblot analysis of CK2 substrates in SUM159 and SUM159R cells following CK2 inhibitor (CX-4945, 10 μ M) 3 h treatment. **g**, Immunoblot analysis of pBRD4 and BRD4 in SUM149 cell line treated with different doses of the indicated PP2A inhibitors for 3 h. ACTB was used as loading control. **h**, Immunoblot analysis of pBRD4 and BRD4 in the indicated cell lines treated with different doses of phenothiazine for 6 h. **i**, Immunofluorescence analysis of exogenous Flag-tagged BRD4 proteins (WT, BD, 7D and 7A) in SUM159 cells with or without JQ1 treatment (5 μ M, 3 h). Scale bars, 20 μ m. For gel source data, see Supplementary Fig. 1.

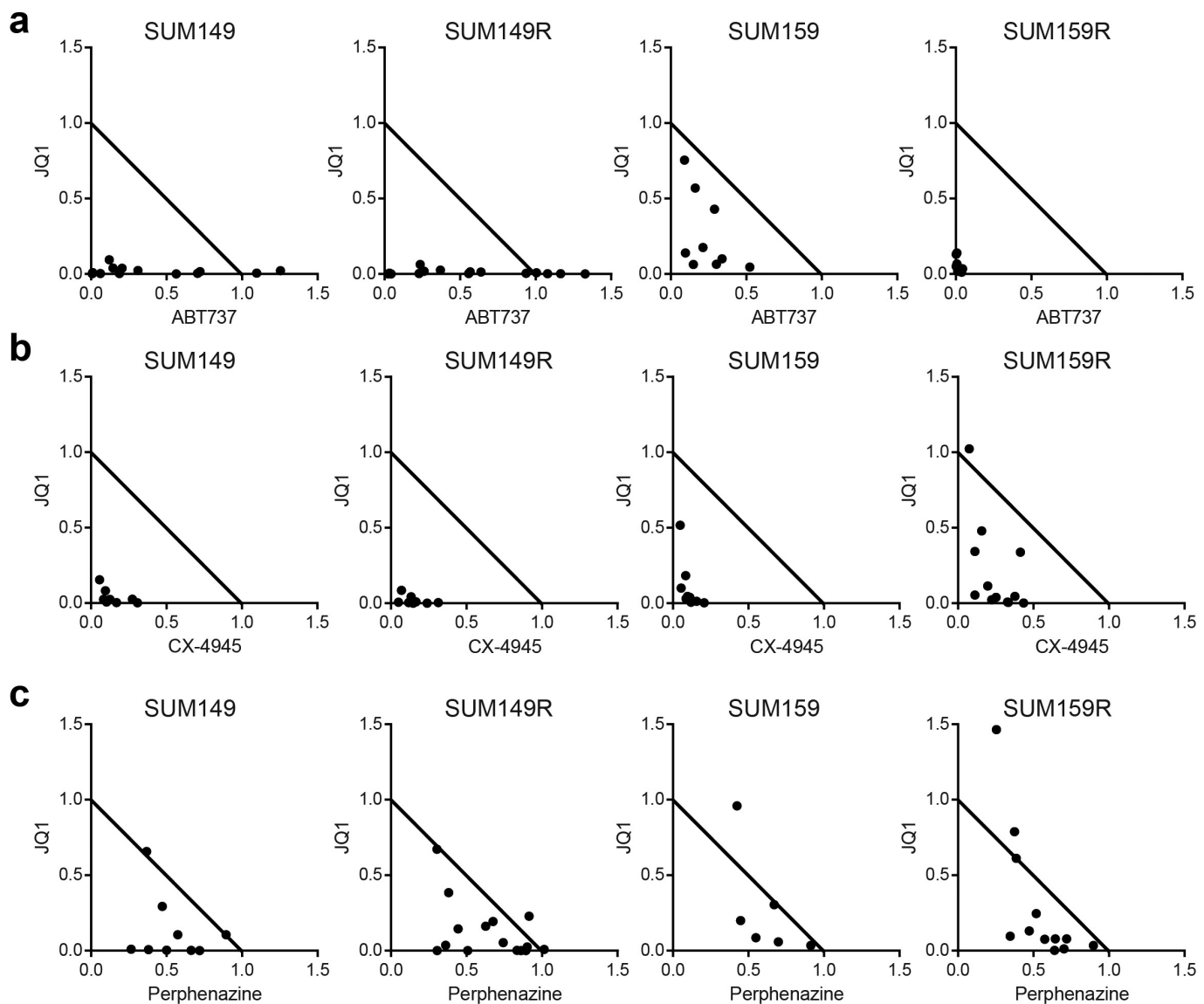
f, Immunoblot analysis of CK2 substrates in SUM159 and SUM159R cells following CK2 inhibitor (CX-4945, 10 μ M) 3 h treatment. **g**, Immunoblot analysis of pBRD4 and BRD4 in SUM149 cell line treated with different doses of the indicated PP2A inhibitors for 3 h. ACTB was used as loading control. **h**, Immunoblot analysis of pBRD4 and BRD4 in the indicated cell lines treated with different doses of phenothiazine for 6 h. **i**, Immunofluorescence analysis of exogenous Flag-tagged BRD4 proteins (WT, BD, 7D and 7A) in SUM159 cells with or without JQ1 treatment (5 μ M, 3 h). Scale bars, 20 μ m. For gel source data, see Supplementary Fig. 1.



Extended Data Figure 9 | See next page for figure caption.

Extended Data Figure 9 | Phospho-BRD4 levels in xenografts and primary TNBC samples. **a**, Immunofluorescence analysis of phospho-BRD4 (pBRD4) in SUM159 parental and SUM159R xenografts showing that resistance is associated with higher pBRD4 levels. **b**, Examples of pBRD4 immunofluorescence in patient tumours depicting variability among different TNBC samples. Scale bars, 50 μm. **c**, Mean intensity of phospho-BRD4 (pBRD4) in tissue samples from 83 patients with early-stage triple negative breast cancer (TNBC). **d**, Examples of androgen receptor and basal cytokeratin (bCK, HMW CK) immunofluorescence in TNBC samples. Scale bars, 50 μm. **e**, Box plot depicting pBRD4 signal intensity in TNBCs tumours with the indicated androgen receptor and bCK expression patterns. None of the differences among groups were

significant (ANOVA test $P = 0.5413$ and Dunnett's multiple comparisons test was not significant). **f**, Kaplan–Meier estimates of disease-free survival (DFS) and overall survival (OS) in TNBC subgroups using a median-split of pBRD4 intensity. Disease outcomes were evaluated in 83 of 89 TMA samples. Patients with low pBRD4 had a worse overall prognosis with a five-year RFS of 66.2% (95% confidence interval (CI) 52.7–83.1%), compared to an RFS of 86.4% (95% CI 76.0–98.3%) among patients with high pBRD4 (HR = 2.3, 95% CI 0.98–5.4, $P = 0.06$). However, with this small sample size this difference did not reach statistical significance, nor did the association of pBRD4 status and overall survival (HR = 2.0, 95% CI 0.67–5.9, $P = 0.22$).



Extended Data Figure 10 | Overcoming BBI-resistance. a–c, Synergy studies of JQ1 with ABT737 (BCL-xL and BCL-2 inhibitor) (a), CX-4945 (CK2 inhibitor) (b) and perphenazine (PP2A activator) (c). Points represent paired values of drug concentrations assessed for synergism.

The diagonal line signifies drug additivity. Points above the line represent antagonistic drug combinations, and those below the line represent synergistic drug combinations.